Journal of Nanobiotechnology

RESEARCH

Open Access

Co-delivery of axitinib and PD-L1 siRNA for the synergism of vascular normalization and immune checkpoint inhibition to boost anticancer immunity

Yanhong Liu[1,3†], Liming Gong[1,4†], Jing Feng[1,4], Congcong Xiao[1,4], Chenfei Liu[1,4], Bohan Chen[1,4], Liqing Chen[1,4], Mingji Jin[1,4], Youyan Guan[2*], Zhonggao Gao[1,4*] and Wei Huang[1,4*]

Abstract

Immune checkpoint inhibition (ICI) has become the mainstay of immunotherapy for the treatment of renal cell carcinoma (RCC). However, only a small portion of patients exhibit a positive response to PD-1/PD-L1 blockade therapy and the key reason is that RCC belongs to a vascular-rich tumor for promoting immunosuppression. Specifically, the dysfunctional tumor vasculature hinders effector T cell infiltration and induces immunosuppressive tumor microenvironment via the release of cytokine, which attenuates the therapeutic efficacy of ICI. Therefore, regulating abnormal tumor vasculature may be a promising strategy to overcome the immunosuppressive microenvironment and enhance ICI therapy. Here, we propose an NGR peptide-modified actively targeted liposome (Axi/siRNA^{PD-L1}@NGR-Lipo) to encapsulate the anti-angiogenic agents Axitinib and PD-L1 siRNA to promote tumor vasculature normalization and relieve immune evasion for enhanced anti-tumor immunotherapy. With NGR-mediated tumor homing and active targeting, Axi/siRNA^{PD-L1}@NGR-Lipo could act on tumor vascular endothelial cells to inhibit neo-angiogenesis, increase pericyte coverage and vascular perfusion, and normalize the structure and function of tumor blood vessels. Meanwhile, it also enhanced immune effector T cells and NK cells infiltration and reduced the proportion of immunosuppressive T cells including MDSC cells and Tregs, thus improving the tumor immunosuppressive microenvironment. Moreover, Axi/siRNA^{PD-L1}@NGR-Lipo reduced the expression of PD-L1 protein in tumor cells, restored the recognition and killing ability of cytotoxic T cells, and relieved immune evasion. As expected, Axi/siRNA^{PD-L1}@NGR-Lipo displayed superior anti-tumor and anti-metastatic efficacy in mice bearing RCC. Overall, this study demonstrated the important potential of regulating abnormal tumor vasculature to

†Yanhong Liu and Liming Gong contributed equally to this work.

*Correspondence:
Youyan Guan
guanyouyan@cicams.ac.cn
Zhonggao Gao
zggao@imm.ac.cn
Wei Huang
huangwei@imm.ac.cn

Full list of author information is available at the end of the article

reshape the immunosuppressive microenvironment and boost ICI therapy, which represents a promising avenue for the synergistic anti-tumor with cancer immunotherapy.

Graphical Abstract

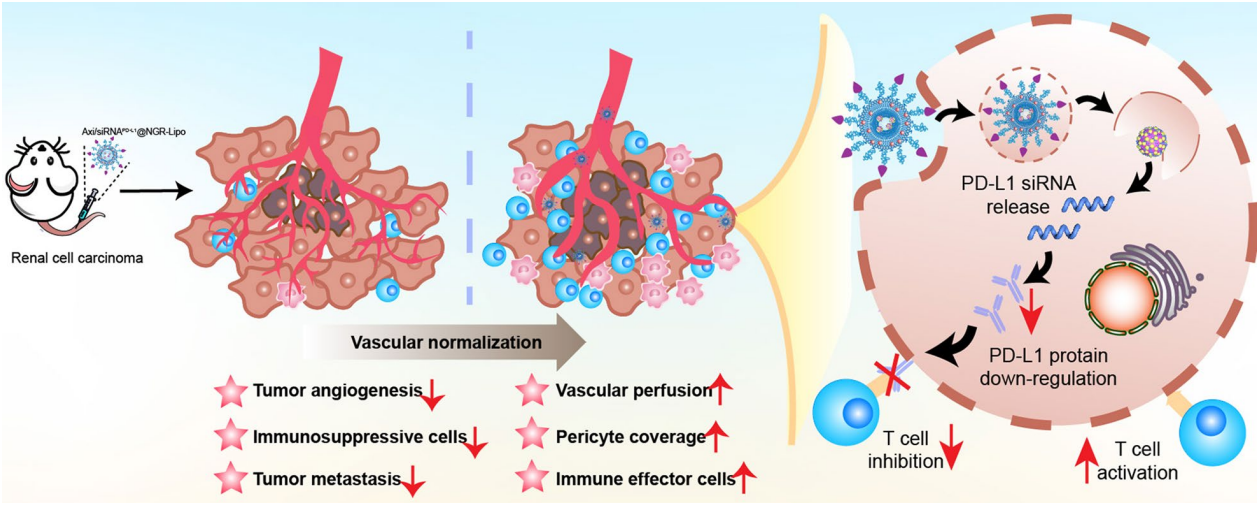

Keywords Immunosuppressive microenvironment, Immune checkpoint inhibition, Vascular normalization, Anti-tumor immunotherapy, Renal cell carcinoma

Introduction

Renal cell carcinoma (RCC) is a malignant cancer commonly occurring in the urinary system, with the incidence increasing over the past decade, only preceded by prostate cancer and bladder cancer [1–3]. Currently, radical surgery stands as the main effective treatment for early-stage RCC patients, with more than 90% five-year survival [4]. However, due to the insidious nature of the disease and the lack of specific markers, most RCC patients are often diagnosed at an advanced stage, with survival rates of only 12% [5]. Patients with advanced RCC primarily rely on systemic drug therapy, but conventional chemotherapeutic agents are rarely effective in advanced RCC [6]. Therefore, there is an urgent demand for a new therapeutic approach to prolong the survival of patients with advanced RCC.

RCC is a vascular-rich tumor in which angiogenesis plays an important role in tumor development and metastasis [7]. Blood vessels provide oxygen and nutrients for tumor growth and also support the metastasis of tumor cells from the primary site to distant tissues and organs [8]. However, the immature neo-vascular system at the tumor site is usually malformed and dysfunctional, characterized by a disorganized microvascular network, defective endothelial cells and sparse pericyte coverage [9–12]. The abnormal vascular system could lead to a high-pressure, acidic and hypoxic tumor microenvironment. More and more studies have found that angiogenesis play an important role in promoting immune evasion of tumor [13]. On the one hand, the abnormal structure and function of the neo-vasculatures impede the infiltration of cytotoxic T lymphocytes (CTL) into tumors, which is a prerequisite for an efficient anti-tumor immune response [14]. Meanwhile, neo-vasculatures typically suffer from the absence of some adhesion molecules, such as vascular cell adhesion molecule-1 (VCAM-1), whose down-regulation further impairs T cell extravasation [14]. On the other hand, VEGF, as a key stimulator of angiogenesis [15, 16], would interfere with the immune response by inhibiting the maturation of dendritic cells (DCs) and increasing the populations of regulatory T cells (Tregs) and myeloid-derived suppressor cells (MDSCs) within the tumor [17, 18]. VEGF was also found to suppress T cell formation and function and promote T cell depletion by upregulating immune checkpoints [19, 20]. Therefore, the aberrant tumor neo-vascular system constitutes a primary physical and biochemical barrier to T cell infiltration and function, thus compromising immunotherapy efficacy [11, 21]. From this, tumor neo-vasculatures are the potential target for the treatment of RCC.

Anti-angiogenic therapy is an emerging therapy for tumors in recent years, which normalizes the tumor vasculature by inhibiting neo-vascularization, thus improving TME and increasing drug penetration. Anti-angiogenic agents (AAs) have become first-line agents in tumor treatment by blocking the interaction of angiogenic factors with their receptors to inhibit tumor

angiogenesis for preventing further cancer progression [22]. Although FDA-approved AAs, including axitinib, pazopanib, bevacizumab, sunitinib, and thalidomide, have exhibited outstanding therapeutic efficacy, there are still risks of poor efficacy, drug resistance, long treatment period, and susceptibility to recurrence in solid tumors [23–25]. Consequently, a single anti-angiogenic therapy is no longer sufficient for the treatment of malignant tumors with complex development processes and drug resistance mechanisms, but the combination of multiple therapies will be required to achieve much more effective therapeutic efficacy.

Immunotherapy, represented by immune checkpoint inhibitors (ICI), has provided unprecedented benefits in the treatment of a wide range of malignancies [26, 27]. Nevertheless, the low immunogenicity of tumor cells and the individual variability of the immune system lead to the fact that usually only a small proportion of patients benefit from ICI [28–30]. The intrinsic nature of ICI therapies only relieves the immune evasion of tumor cells, so even if PD-1/PD-L1 binding is blocked, less CTL infiltration arising from the abnormal vascular system in tumors may result in weak immune response activation. From this perspective, the combination of anti-angiogenic therapy and ICI seems to be a match made in heaven, where AAs normalize the vasculature and increase CTL infiltration, in parallel with ICI that disarms the immune evasion of tumor cells, with both therapies potentiating the immune response synergistically. Furthermore, it has also been shown that ICI can enhance the efficacy of AAs by promoting vascular changes [11]. For example, Tian et al. found that depletion or deactivation of $CD4^+$ T cells reduced vascular normalization, whereas ICI activation improved tumor vascular normalization [31]. Hence, anti-angiogenic therapies and ICI are complementary and mutually reinforcing in their mechanisms of action, and have great potential for combined application in RCC treatments.

In this study, we designed NGR peptide-modified actively targeted liposomes (Axi/siRNA^{PD-L1}@NGR-Lipo) to co-encapsulate Axitinib (Axi) and siRNA^{PD-L1} for the synergism of anti-angiogenic therapies and ICI for the treatment of RCC (Scheme 1). NGR peptide could provide tumor-homing and active targeting effects by binding to CD31 overexpressed in the surface of tumor cells and tumor neo-vasculature. After specific accumulation in the tumor tissue, Axi/siRNA^{PD-L1}@NGR-Lipo was endocytosed by tumor cells and tumor vascular endothelial cells to release Axi and siRNA^{PD-L1}. On the one hand, the anti-angiogenic drug Axi inhibited the generation of tumor neo-vasculatures and normalized the tumor vascular system to promote CTL infiltration. On the other hand, the released siRNA^{PD-L1} suppressed the PD-L1 gene to reduce the expression of the PD-L1 proteins on the surface of tumor cells, thus relieving the immune evasion of tumor cells. During the research, it was shocking to find that Axi alone induced an elevation of the PD-L1 protein on the surface of tumor cells, which could lead to severe immune evasion. Nevertheless, it also provides additional imperative and rationale for the combination of Axi with siRNA^{PD-L1}, as Axi/siRNA^{PD-L1}@NGR-Lipo significantly reduced PD-L1 proteins on the surface of tumor cells and improved anti-tumor immune efficacy. Overall, this study provides a novel approach for the application of the combination of anti-angiogenic therapy and ICI in the treatment of RCC, with potential clinical translation and application.

Results and discussion

Preparation and characterization of Axi/siRNAPD–L1@NGR-Lipo

Firstly, DSPE-PEG2000-NGR was obtained by the thiolene "click" reaction of the maleimide group in DSPE-PEG2000-MAL and the sulfhydryl group on the cysteine at the end of the NGR peptide (Fig. S1). The ^{1}H-NMR spectrum demonstrated that the characteristic peak of maleimide at 6.8 ppm was present in the spectrum of DSPE-PEG2000-MAL, while disappearing in DSPE-PEG2000-NGR (Fig. S2), indicating the successful conjugation of the maleimide group to sulfhydryl group. The MALDI-TOF results presented that the major peaks of DSPE-PEG2000-MAL, NGR and DSPE-PEG2000-NGR were 2275.4, 783.31 and 2872.8, respectively, which were substantially consistent with the theoretical molecular weights, thus further indicating the successful synthesis of DSPE-PEG2000-NGR (Fig. S3).

Subsequently, Pro-siRNA^{PD-L1} complexes were formed by self-assembly via the charge interaction of protamine with siRNA^{PD-L1}. The results of agarose gel electrophoresis revealed that siRNA^{PD-L1} could be completely solidified when the mass ratio of protamine to siRNA^{PD-L1} exceeded 3:1 (Fig. 2A). As the mass ratio increased, although siRNA^{PD-L1} was fully consolidated, the particle size of the Pro-siRNA^{PD-L1} complexes also became too large to satisfy the size of nanocore (Fig. 2B). Hence, the mass ratio of protamine to siRNA^{PD-L1} was 3:1 as the optimum ratio for the preparation of Pro-siRNA^{PD-L1} complexes.

Next, Axi was encapsulated in liposomes by thin-film dispersion, and eventually, Axi/siRNA^{PD-L1}@NGR-Lipo was obtained by co-extruding liposomes with Pro- siRNA^{PD-L1} complexes using a lipid extruder. The average size and particle size distribution of the prepared nanoparticles were measured by dynamic light scattering (DLS). The average particle sizes of Pro-siRNA^{PD-L1}, Axi/siRNA^{PD-L1}@Lipo and Axi/siRNA^{PD-L1}@NGR-Lipo were 120.1 nm, 159.8 nm and 156.2 nm, with PDI of 0.260, 0.109 and 0.156, respectively (Fig. 2C). Additionally, DLS

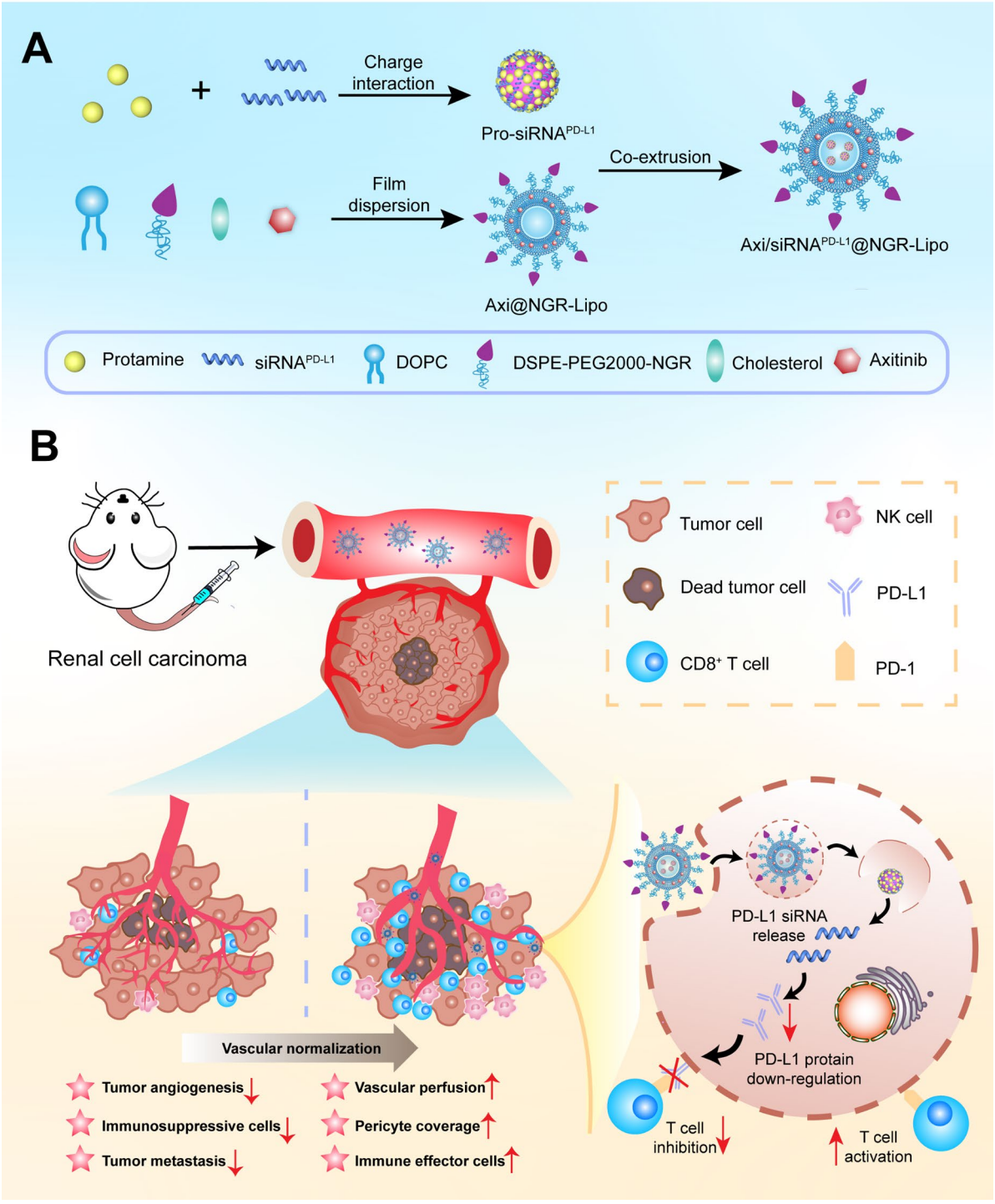

Fig. 1 Construction of NGR peptide-modified actively targeted liposomes Axi/siRNA^{PD-L1}@NGR-Lipo co-encapsulating Axi and siRNA^{PD-L1} and mechanism of combining anti-angiogenic and ICI therapies to enhance anti-tumor immunotherapy for the treatment of renal cell carcinoma

measurements of zeta potential displayed that the surface potentials of Pro-siRNA^{PD-L1}, Axi/siRNA^{PD-L1}@Lipo and Axi/siRNA^{PD-L1}@NGR-Lipo were 13.53 mV, -7.88 mV and -14.13 mV, respectively (Fig. 2E). The encapsulation of Pro-siRNA^{PD-L1} by liposomes shifted the surface charge from positive to negative but with little change in particle size, which enabled remarkable stability in vivo and prolonged the period of circulation. To more intuitively identify the microstructure of the nanoparticles, transmission electron microscopy (TEM) was adopted to observe their surface morphology. Pro-siRNA^{PD-L1} displayed irregular spheres, whereas Axi/siRNA^{PD-L1}@Lipo

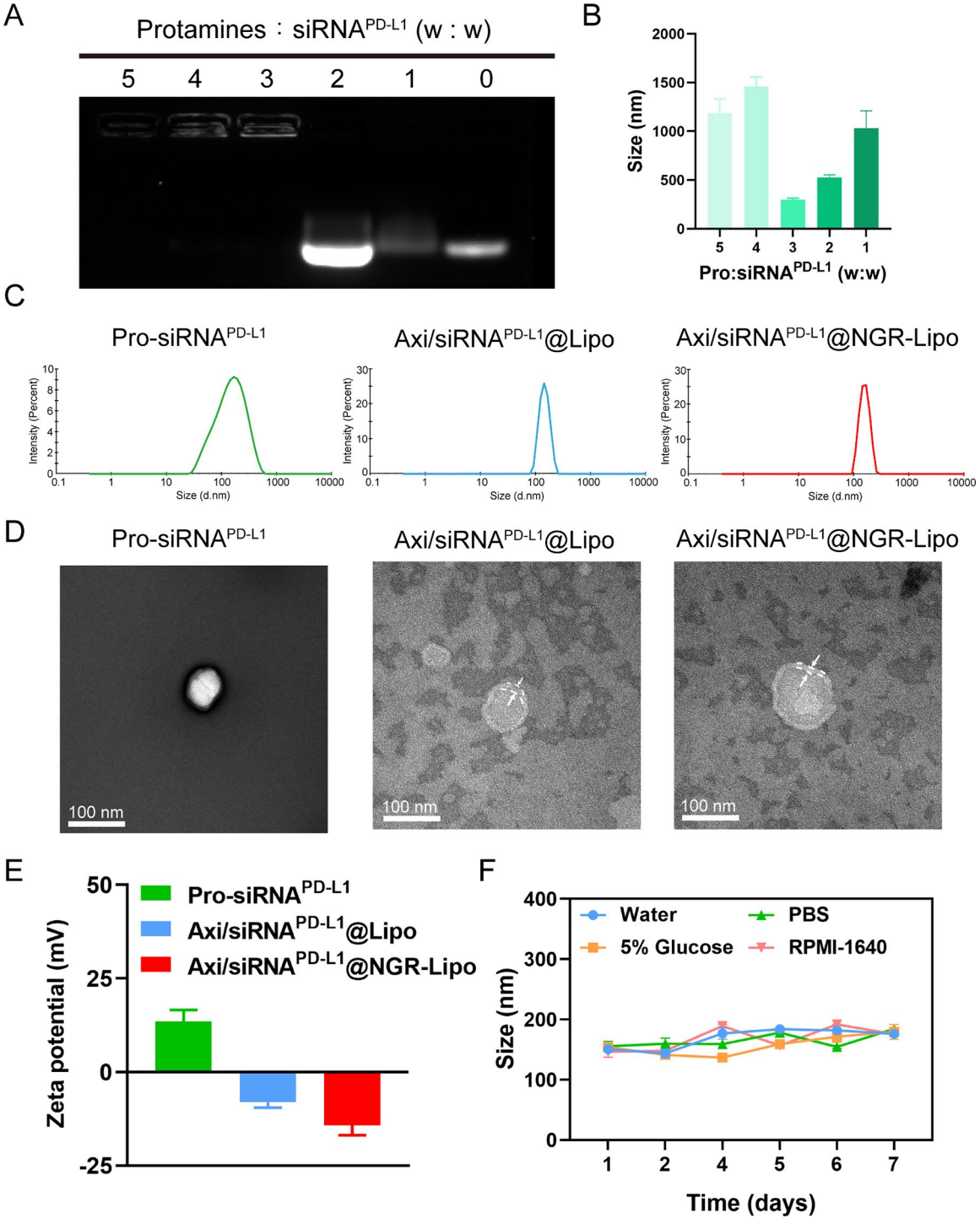

Fig. 2 Characterization of various preparations. (**A**) Agarose gel electrophoresis assays of Pro-siRNA^{PD-L1} at different mass ratios. (**B**) Particle sizes of Pro-siRNA^{PD-L1} at different mass ratios. (**C**) Particle size distribution (**D**) Transmission electron microscopy (TEM) images and (**E**) Zeta potential of Pro-siRNA^{PD-L1}, Axi/siRNA^{PD-L1}@Lipo and Axi/siRNA^{PD-L1}@NGR-Lipo. (**F**) Storage stability of Axi/siRNA^{PD-L1}@NGR-Lipo in water, PBS, 5% glucose and RPMI-1640 for 7 days. ($n = 3$)

and Axi/siRNA^{PD-L1}@NGR-Lipo presented a distinct "core-shell" structure (Fig. 2D). The above results comprehensively demonstrated the successful preparation of Axi/siRNA^{PD-L1}@NGR-Lipo. Consequently, the colloidal stability of Axi/siRNA^{PD-L1}@NGR-Lipo was characterized by investigating the change of particle size during 7 days of storage in water, PBS, 5% glucose and RPMI-1640. As shown in Fig. 2F and Fig. S4, the nanoparticles

are well stabilized as the particle size is below 200 nm for 7 days in different media and the particle size was no apparent change, with the rate of change within a 20% range. These results indicated outstanding storage stability of the nanoparticles.

In vitro cellular uptake assays

The effective cellular uptake is the prerequisite for therapeutic efficacy of agents. As such, Cou-6 as a fluorescent reagent was encapsulated in liposomes instead of Axi to investigate the efficiency of cellular uptake by HUVEC cells and Renca cells. As shown in Figs. S5 and S6, the cellular uptake of Axi/siRNA^{PD-L1}@NGR-Lipo by HUVEC cells and Renca cells both gradually increased with the extension of incubation time, presenting a time-dependent pattern. Then, the cellular uptake of different formulations by HUVEC cells was visualized by CLSM. As shown in Fig. 3A, Cou-6@NGR-Lipo displayed a more intense green fluorescence signal than free Cou-6 and Cou-6@Lipo, suggesting that NGR promoted the cellular uptake of nanoparticles by CD13-overexpressing HUVEC cells. However, after pre-incubation with free NGR peptide to saturate the receptor, an obvious decrease of green fluorescence was observed in the Cou-6@NGR-Lipo group, whereas Cou-6@Lipo exhibited no significant alteration, evidencing the mechanism that nanoparticles

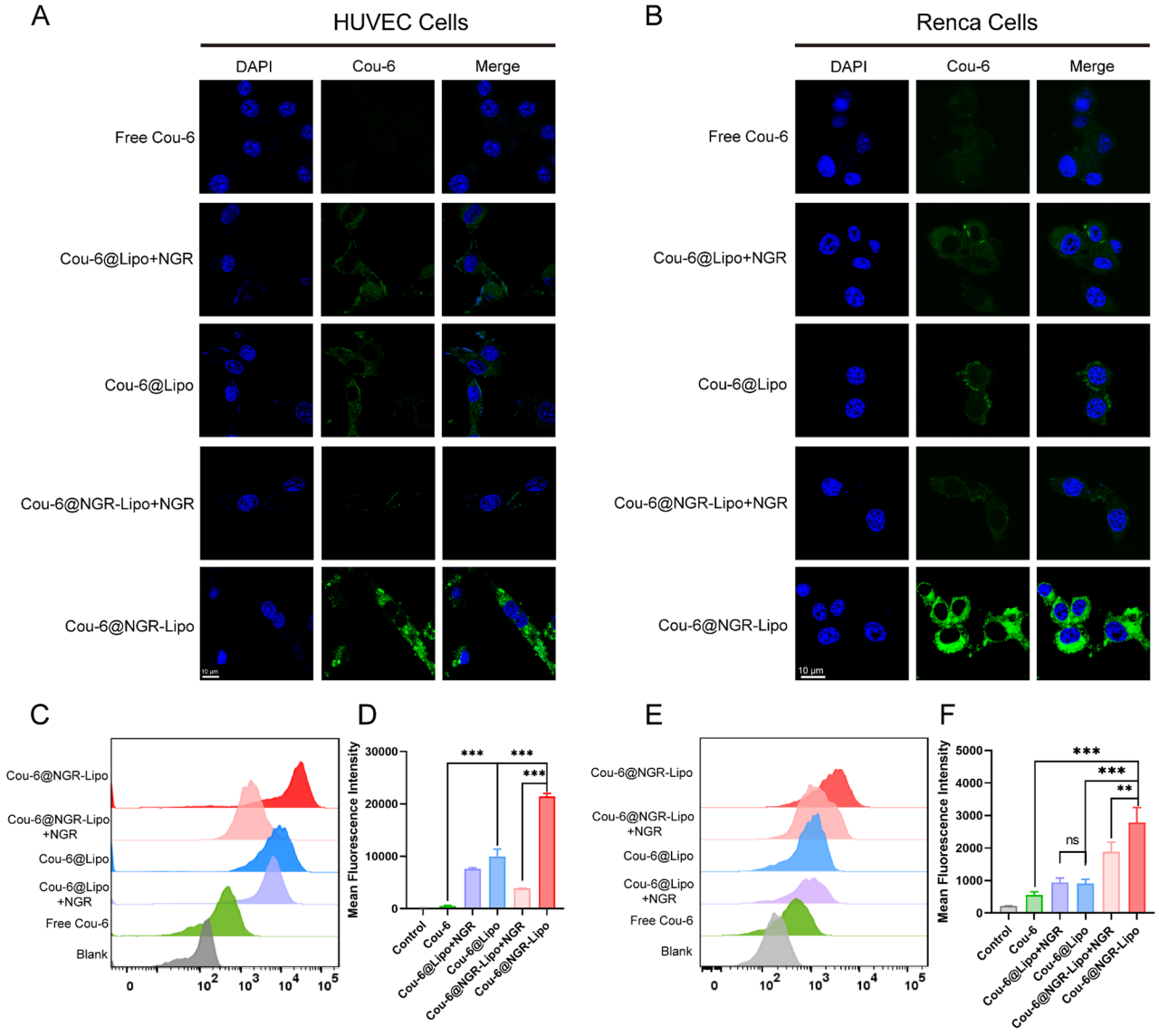

Fig. 3 Cellular uptakes in HUVEC cells and Renca cells. Confocal microscopy images of cellular uptakes of various formulations in HUVEC cells (**A**) and Renca cells (**B**). (**C**) Flow cytometry analysis and (**D**) Quantitative analysis of cellular uptakes of various formulations in HUVEC cells. (**E**) Flow cytometry analysis and (**F**) Quantitative analysis of cellular uptakes of various formulations in Renca cells. Data were present as mean ± SD ($n = 3$). $^{**}p < 0.01$, $^{***}p < 0.001$

are engaged into the cell via an endocytosis pathway mediated by NGR binding to the CD13 receptor. Quantitative analysis by flow cytometry followed the same trend as CLSM, with the mean fluorescence intensity of Cou-6@NGR-Lipo in HUVEC cells appearing 40.4-fold, 2.15-fold and 5.53-fold higher than that of free Cou-6, Cou-6@Lipo and Cou-6@NGR-Lipo + NGR, respectively (Fig. 3C and D). Moreover, when investigating the cellular uptake of nanoparticles by Renca cells, CLSM images revealed the similar phenomenon appeared in HUVEC cellular uptake assays, with Cou-6@NGR-Lipo displaying a more intense fluorescent signal than any other groups (Fig. 3B). Quantitative analysis by flow cytometry displayed that the mean fluorescence intensity of Renca cells treated with Cou-6@NGR-Lipo was 5.05-fold, 3.06-fold and 1.48-fold higher than that of free Cou-6, Cou-6@Lipo and Cou-6@NGR-Lipo + NGR, respectively (Fig. 3E and F). The above results suggested that NGR-modified liposomes could significantly enhance cellular uptake by HUVEC cells and Renca cells by binding to the overexpressed CD13 receptor.

In vitro gene silencing and anti-tumor efficiency

It has been reported that PD-L1 protein could inhibit T cell-mediated immune response, promote the exhaustion of effector T cells and cause immune evasion of tumor cells through binding to PD-1 expressed on activated T cells [32, 33]. PD-L1 expression is regarded as a predictive biomarker of response to ICI therapies. Here, we carried out western blot assays to explore whether the treatments of the anti-angiogenic drug Axi alone influence the PD-L1 expression on the surface of Renca cells. Astonishingly, from Fig. 4A, we found that the expression of PD-L1 protein on the surface of Renca cells was gradually elevated with the concentrations of Axi increasing. The enhanced tumor PD-L1 expression could potentially be used to sensitize tumors to ICI therapies, which provided a strong rationale for the combination of Axi with siRNA^{PD-L1}. This similar phenomenon was also found in the previously reported studies [34]. Subsequently, we investigated the effects of different preparations including Control, Axi, siRNA^{PD-L1}, Axi/siRNA^{PD-L1}@Lipo and Axi/siRNA^{PD-L1}@NGR-Lipo on PD-L1 proteins on the surface of Renca cells (Fig. 4B). Similar to the above results, free Axi caused a slight increase in the expression of PD-L1 protein. Compared with free siRNA, both Axi/siRNA^{PD-L1}@Lipo and Axi/siRNA^{PD-L1}@NGR-Lipo decreased the expression of PD-L1 protein as expected, with Axi/siRNA^{PD-L1}@NGR-Lipo silencing PD-L1 protein most efficiently. Thus, Axi/siRNA^{PD-L1}@NGR-Lipo provided potent efficacy and substantial advantages in reducing PD-L1 protein on the surface of Renca cells.

Next, we investigated the toxicity and growth inhibition of different agents on HUVEC cells and Renca cells. The IC50 values of free Axi, Axi/siRNA^{PD-L1}@Lipo and Axi/siRNA^{PD-L1}@NGR-Lipo were 24.36 μg/mL, 17.37 μg/mL and 6.60 μg/mL for HUVEC cells and 39.47 μg/mL, 25.45 μg/mL and 10.95 μg/mL for Renca cells, respectively, as determined by CCK-8 assay, and all of them presented a dose-dependent toxicity (Fig. 4C and D). Axi/siRNA^{PD-L1}@NGR-Lipo displayed the highest cytotoxicity for HUVEC cells and Renca cells, which may be attributed to the higher NGR-mediated cellular uptake. Additionally, Annexin V-FITC/PI staining was performed to examine the induction of apoptosis in HUVEC cells and Renca cells by different preparations. For HUVEC cells, Axi/siRNA^{PD-L1}@NGR-Lipo induced the most apoptosis, with the percentage of apoptotic cells in free Axi, Axi/siRNA^{PD-L1}@Lipo and Axi/siRNA^{PD-L1}@NGR-Lipo reaching 33.77%, 45.22% and 66.4%, respectively (Fig. 4E and F). A similar trend also occurred on Renca cells, where the percentage of apoptotic cells induced by free Axi, Axi/siRNA^{PD-L1}@Lipo and Axi/siRNA^{PD-L1}@NGR-Lipo was 6.58%, 28.27% and 33.5%, respectively (Fig. 4G and H). Furthermore, in live/dead cell staining assays, cells treated with Axi/siRNA^{PD-L1}@NGR-Lipo appeared to exhibit substantial red fluorescence (dead cells) in HUVEC cells (Fig. 4I) and Renca cells (Fig. 4J). Taken together, Axi/siRNA^{PD-L1}@NGR-Lipo demonstrated elevated cytotoxicity and excellent capacity to induce apoptosis on both HUVEC and Renca cells, which gave confidence for subsequent in vivo efficacy studies.

Penetration and growth inhibition of 3D spheroids in vitro

Although the above results have demonstrated that Axi/siRNA^{PD-L1}@NGR-Lipo could enhance cytotoxicity on Renca cells and effectively induce apoptosis, the 2D cell culture could not actually mimic the tumor tissue [35, 36]. Thus, we constructed 3D tumor spheres with Renca cells to more accurately mimic tumor tissue, which were subsequently taken to study the penetration and growth inhibition of NGR-modified liposomes. After 12 h of co-incubation with 3D tumor spheres, the Cou-6@NGR-Lipo group displayed much more intense fluorescence intensity and deeper penetration compared with free Cou-6 and Cou-6@Lipo group, which may be related to the NGR-mediated targeting capacity and endocytosis (Fig. 5A). Subsequently, within 7 days of investigating growth inhibition on tumor spheres, compared to free Axi group, tumor spheres in the liposome group both became remarkably smaller and even collapsed, with the most severe disintegration occurring in Axi/siRNA^{PD-L1}@NGR-Lipo group (Fig. 5B). This phenomenon would probably be attributed to the elevated cytotoxicity of Axi/siRNA^{PD-L1}@NGR-Lipo due to increased cellular uptake mediated by NGR, which leads to apoptosis of the outer cells, gradually shrinking the tumor spheres or even failing to maintain the sphere morphology.

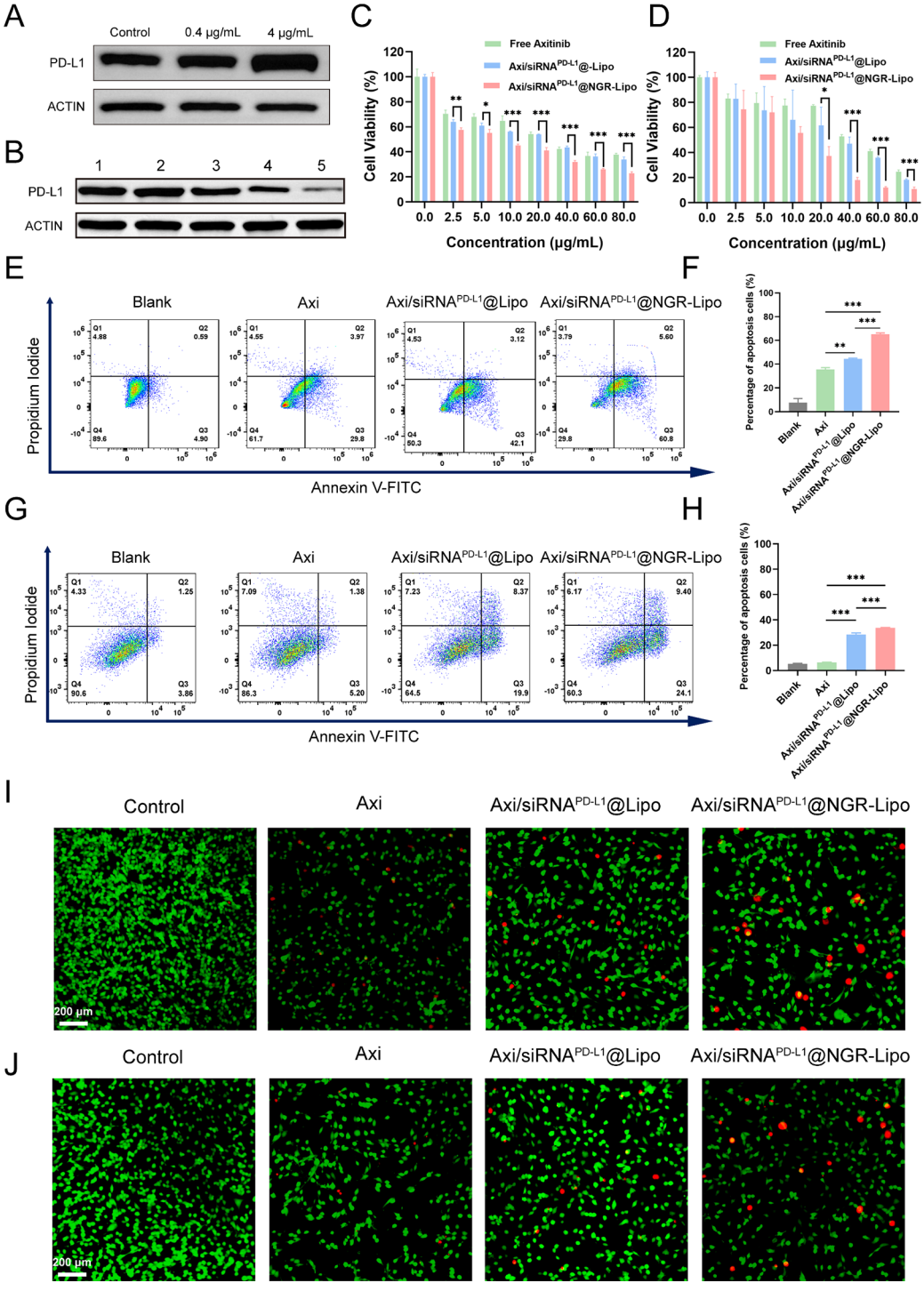

Fig. 4 In vitro gene silencing and anti-tumor studies. (**A**) Western blot (WB) analysis of PD-L1 protein in Renca cells treated with Axitinib of different concentrations. (**B**) WB analysis of PD-L1 protein in Renca cells treated with various formulations. (1: Control, 2: Axi, 3: siRNA^{PD-L1}, 4: Axi/siRNA^{PD-L1}@Lipo, 5: Axi/siRNA^{PD-L1}@NGR-Lipo.) Cytotoxicity of Free Axi, Axi/siRNA^{PD-L1}@Lipo and Axi/siRNA^{PD-L1}@NGR-Lipo of different concentrations on HUVEC cells (**C**) and Renca cells (**D**) ($n = 4$). Flow cytometry assay (**E**) and quantitative analysis (**F**) of apoptotic HUVEC cells treated with various formulations ($n = 3$). Flow cytometry assay (**G**) and quantitative analysis (**H**) of apoptotic Renca cells treated with various formulations ($n = 3$). Live/dead cell staining of HUVEC cells (**I**) and Renca cells (**J**) after various treatments. Data were present as mean ± SD. *$p < 0.05$, **$p < 0.01$, ***$p < 0.001$

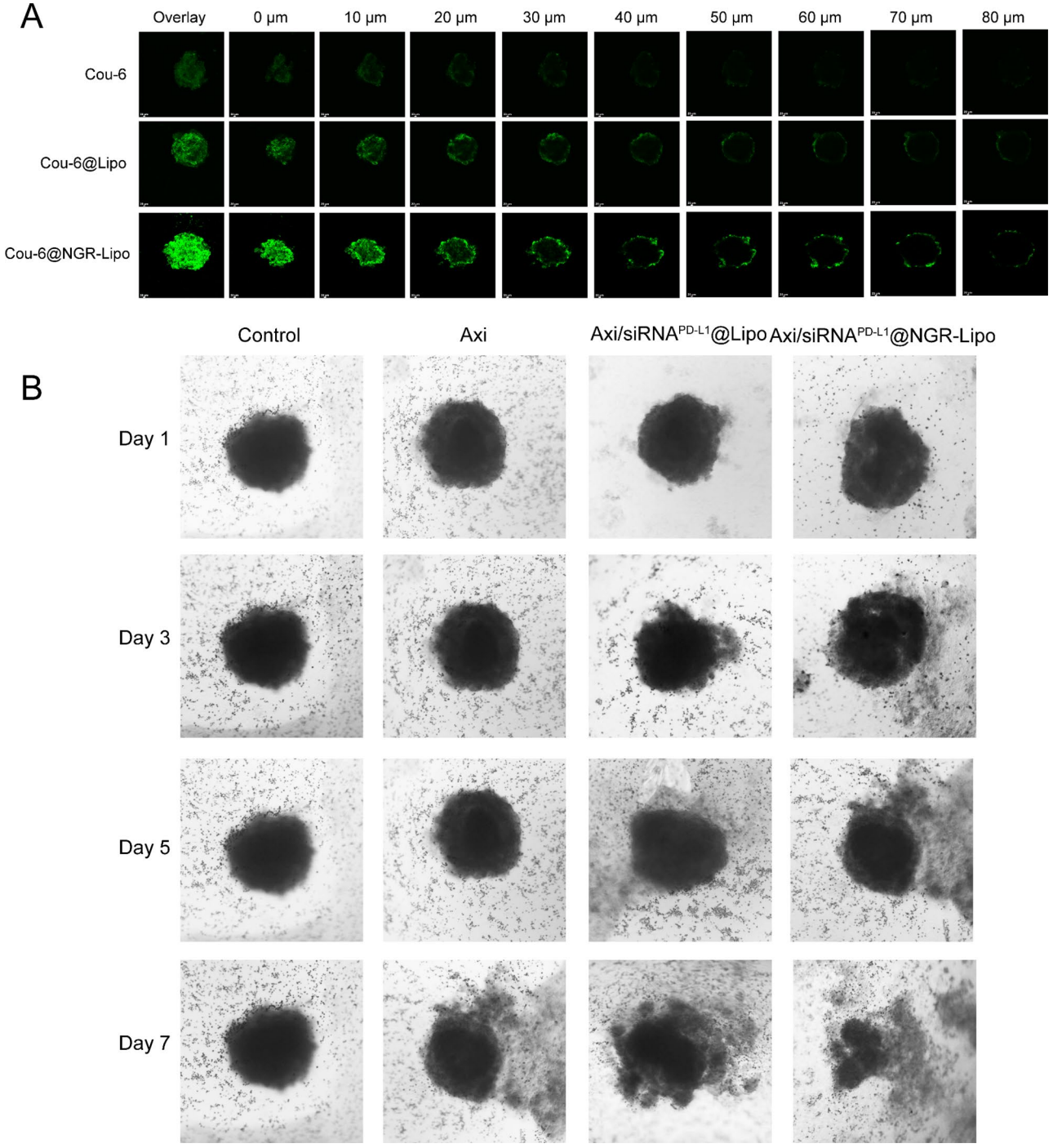

Fig. 5 Penetration and growth inhibition of 3D spheroids in vitro. (**A**) Tumor spheroid uptake after various treatments. (**B**) Representative images of tumor spheroids treated with various preparations within 7 days

In vivo biodistribution and tumor accumulation

The crucial factor for agents to achieve therapeutic efficacy lies in the specific targeting and aggregation at the tumor site in vivo. Subsequently, we explored the biodistribution and tumor aggregation of liposomes through an in vivo imaging system. Mice-bearing subcutaneous Renca tumor were imaged under an in vivo imaging system to observe the fluorescence intensity of tumor tissues at 1 h, 2 h, 4 h, 6 h, 8 h and 24 h after injection of free DiR, DiR@Lipo and DiR@NGR-Lipo, respectively. With the prolongation of time, no fluorescent signals were observed at the tumor site in free DiR group, while the fluorescent signals in the liposome group gradually increased, with DiR@NGR-Lipo group displaying the

strongest fluorescent signal intensity (Fig. 6A). Subsequently, we carried out a quantification of the fluorescence intensity in the tumor. The results demonstrated that the same trend was observed, with the fluorescence intensity at the tumor site in the DiR@NGR-Lipo group being significantly higher than that in the Free DiR and DiR@Lipo groups (Fig. 6C). The results were related to the NGR-mediated tumor homing and active targeting capacity. At 24 h post-injection, major organs (heart, liver, spleen, lungs and kidneys) and tumors of mice were excised for ex vivo organ fluorescence imaging. Tumor tissues of DiR@NGR-Lipo group possessed the strongest fluorescence signals, indicating an elevated aggregation of tumor site (Fig. 6B). Quantitative analysis revealed a similar trend, with the fluorescence intensity in tumor of DiR@NGR-Lipo and DiR@Lipo being 5.42-fold and 4.45-fold higher than that of free DiR, respectively (Fig. 6D). To better assess the accumulation efficiency of nanomaterials in various organs and tumors, we calculated the fluorescence intensity of specific organs relative to the total fluorescence. The results demonstrated that the distribution proportion of DiR@NGR-Lipo in tumor tissues is significantly higher than in other tissues, ranking second only to the liver (Fig. S7). Moreover, compared with Free DiR and DiR@Lipo, DiR@NGR-Lipo treatment improved its accumulation in tumor tissues and reduced its distribution in the liver. Taken together, NGR modification enhances the targeting of liposomes to tumor tissue, allowing more liposomes to accumulate at the tumor site rather than in normal tissues which holds promise for subsequent exploration of anti-tumor efficacy in vivo.

In vivo anti-tumor efficacy and biosafety

Encouraged by the superior anti-tumor efficacy in vitro and tumor-specific aggregation in vivo, we proceeded to investigate the anti-tumor efficacy of Axi/siRNA^{PD-L1}@

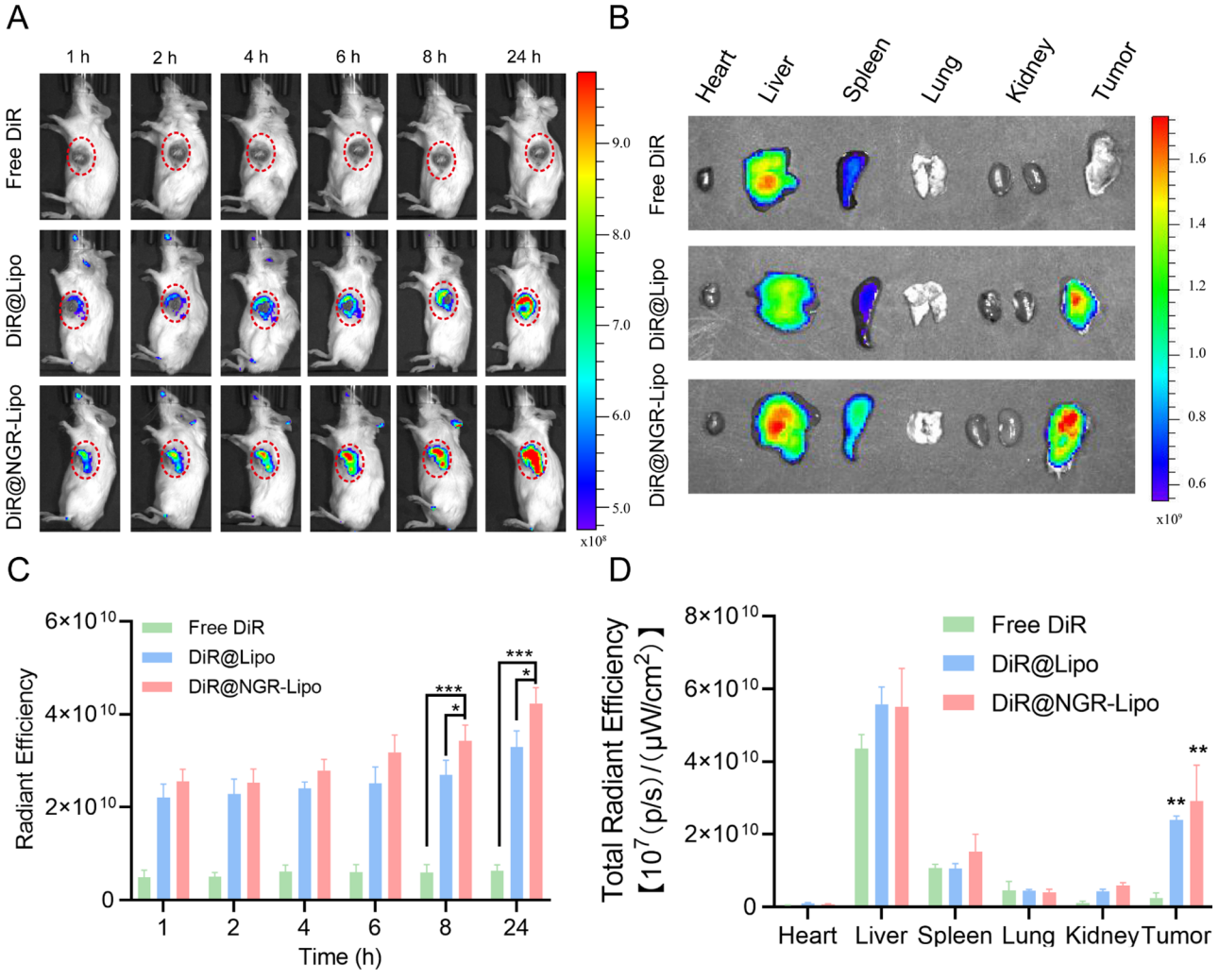

Fig. 6 Biodistribution and tumor accumulation in vivo. (**A**) In vivo fluorescence images of Renca-bearing mice at 1 h, 2 h, 4 h, 6 h, 8 h and 24 h after injection. (**B**) Ex vivo fluorescence images of major organs and tumors at 24 h after injection. (**C**) Quantitative analysis of fluorescence intensity at tumor ($n=3$). (**D**) Quantitative analysis of major organs and tumors ($n=3$). Data were present as mean ± SD. *$p<0.05$, **$p<0.01$, ***$p<0.001$

Lipo in a mouse model with subcutaneous renal tumors. Mice bearing Renca tumor were treated with various preparations for 5 administrations, according to the treatment schedule shown in Fig. 7A. As shown in Fig. 7B and D, during the treatment, tumors in Control group and free Axi group grew rapidly, while Axi@NGR-Lipo group and Axi/siRNA^{PD-L1}@Lipo group displayed slightly slow growth of tumors, indicating that they have anti-tumor efficacy. In contrast, Axi/siRNA^{PD-L1}@NGR-Lipo significantly and effectively controlled tumor growth, suggesting an enhanced anti-tumor effect. At the end of the treatment, the extracted tumor was photographed and weighed (Fig. 7C and E), where the smallest size and lightest weight further validated the superior anti-tumor effect of Axi/siRNA^{PD-L1}@NGR-Lipo. Furthermore, to investigate the effect of liposomes on the survival of mice, another 50 mice with tumors were treated as described above, and the survival of the mice was observed for 60 days. As shown in Fig. 7F, more than half of mice in Axi/siRNA^{PD-L1}@NGR-Lipo group were still alive at 60 days, while all the mice in other groups gradually died, suggesting that Axi/siRNA^{PD-L1}@NGR-Lipo significantly prolonged the survival period of mice bearing tumors.

To further validate the anti-tumor effect of Axi/siRNA^{PD-L1}@NGR-Lipo, hematoxylin and eosin (HE) staining and TdT-mediated dUTP nick-end labelling (TUNEL) staining were performed to evaluate pathological sections of tumors. Axi/siRNA^{PD-L1}@NGR-Lipo exhibited severe nuclear crumpling and deletion, and the most intense apoptotic green fluorescent signals (Fig. 7G), suggesting the potent killing effects on tumor cells. The efficacy of anti-angiogenic agents is not only reflected in the inhibition effect of tumors, but also prevention of the occurrence of tumor metastasis. Hence, lung tissues of mice were excised to observe tumor nodules and perform HE staining for the investigation of tumor metastasis. As can be seen from Fig. 7H, substantial tumor nodules appeared in the lungs of Control group, which were only slightly attenuated in free Axi group. In contrast, the pulmonary metastasis of tumors in the liposome group was significantly reduced, with almost no metastatic tumor nodules found in the lungs of Axi/siRNA^{PD-L1}@NGR-Lipo group, and similar results were also apparent in HE staining of lungs. Consequently, Axi/siRNA^{PD-L1}@NGR-Lipo possessed excellent anti-tumor metastasis capability, which could potentially owe to the outstanding anti-angiogenic properties.

In the case of therapeutic agents, it is not only excellent therapeutic efficacy that is required, but also optimum biosafety. Subsequently, the biosafety of mice in each group was assessed during the treatment. The body weights of the mice in each group experienced no obvious changes during the treatment (Fig. S8). At the end of treatment, serum was collected from the mice for assessment of liver and kidney indices. Serum biochemical levels including ALT, AST, BUN and CRE, were not significantly altered in the treated groups as compared to Control group, indicating no hepatotoxicity or nephrotoxicity (Fig. S9). Moreover, the major organs of the mice (heart, liver, spleen and kidney) were extracted for HE staining. Compared with Control group, there were no abnormal changes in the pathological sections of the other treated groups, indicating that the preparation does not cause significant toxicity and damage to other organs (Fig. S10). Thus, the prepared liposomes have excellent biocompatibility and biosafety, with great potential for the treatment of renal cancer.

Tumor vascular remodeling in vivo

RCC is a vascular-rich tumor, characterized by aberrant structure and function. The abnormal blood vessel network could limit immune cell infiltration into tumors, endogenous immune surveillance and immune cell function, resulting in immune suppressive microenvironment. Regulating tumor vascular has become a promising strategy for improving the efficacy of immunotherapy. Therefore, we would like to investigate Axi/siRNA^{PD-L1}@NGR-Lipo whether could improve the structure and function of the vascular system in the tumor. Treated with various preparations, tumors were extracted for CD31 staining, as a marker of vascular endothelium, and for α-smooth muscle actin (α-SMA) staining, as a marker of pericytes, where pericyte coverage are commonly served as an indicator of vascular function and integrity to identify vessel maturity [37]. Tumors in Control group showed abundant CD31 red fluorescence signals but weak green fluorescence of α-SMA, which indicated that the tumors contained extensive immature microvessels but lacked pericyte coverage around the endothelial walls, with abnormal vascular structure and function (Fig. 8A). The abnormal and chaotic vascular system in the tumor could aggravate the acidic and hypoxic microenvironment, which would promote the invasion, generation, metastasis and immunosuppressive microenvironment of the tumor [7]. In contrast, tumors of Axi/siRNA^{PD-L1}@NGR-Lipo group exhibited significantly reduced CD31 red fluorescence of microvessels and increased α-SMA green fluorescence of pericytes. In particular, there was more co-localization of red CD31 fluorescence and green α-SMA fluorescence, indicating the presence of normal structured and functioning blood vessels. Quantitative analysis also revealed similar results, with 11.3-fold decrease of microvessel density and 7.04-fold elevation of pericyte coverage in tumors of Axi/siRNA^{PD-L1}@NGR-Lipo group as compared to Control group (Fig. 8D and E). The above results indicated that Axi/siRNA^{PD-L1}@NGR-Lipo could effectively remodel and normalize the tumor vascular.

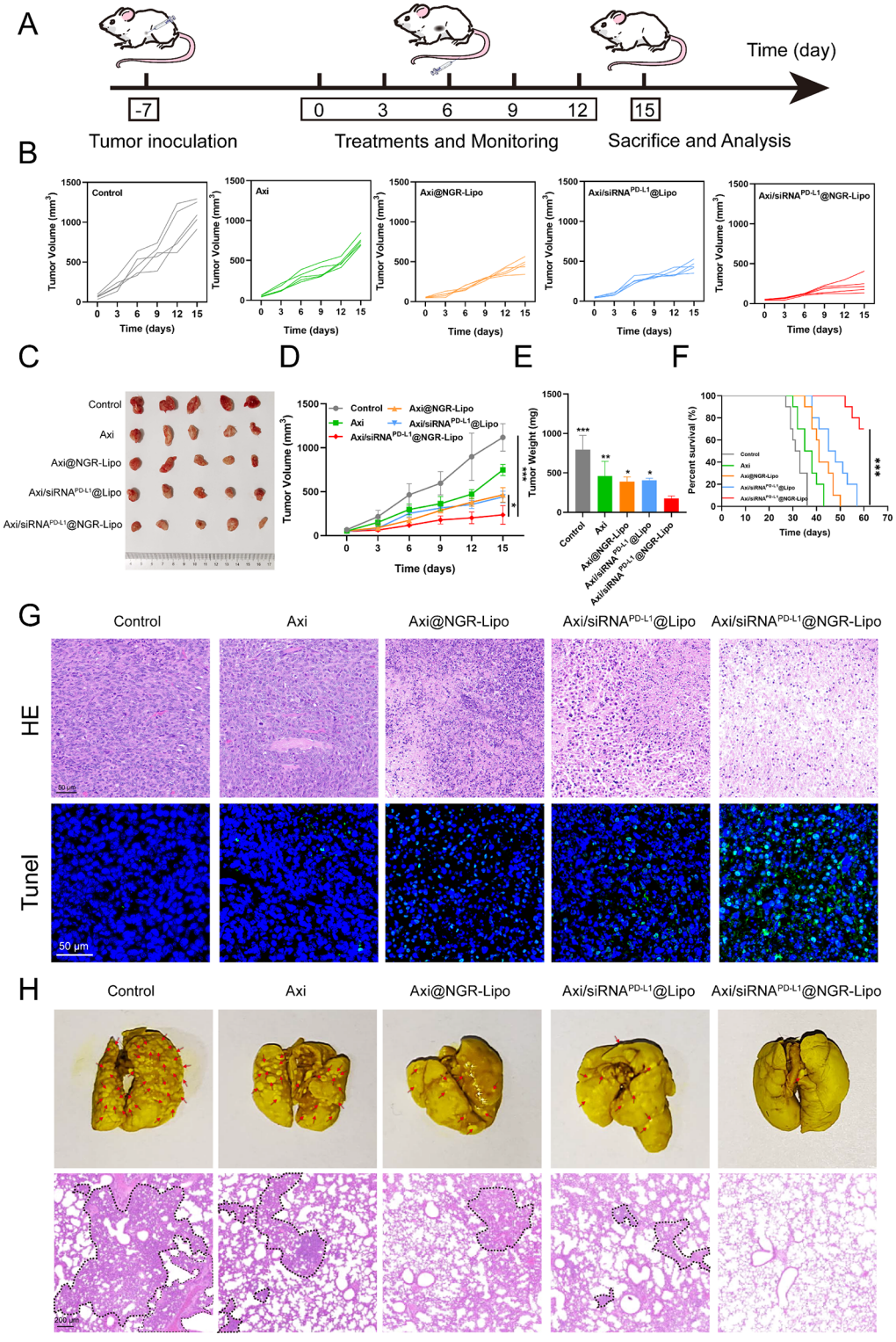

Fig. 7 In vivo anti-tumor and anti-metastasis evaluation. (**A**) Schematic illustration of the treatment. (**B**) Tumor growth curves of each mouse in different groups ($n = 5$). (**C**) Images of the extracted tumors. (**D**) The mean tumor volumes of mice treated with various preparations ($n = 5$). (**E**) Mean weight of isolated tumors ($n = 5$). (**F**) Survival curves of mice treated with various preparations ($n = 5$). (**G**) Images of HE and TUNEL stained tumor sections from each group of mice. (**H**) Lung tissue and HE-stained sections of mice in different groups. Red arrows pointed to lung metastatic tumor nodules. Black dotted line: lung metastatic tumor. Data were present as mean ± SD. $^*p < 0.05$, $^{**}p < 0.01$, $^{***}p < 0.001$

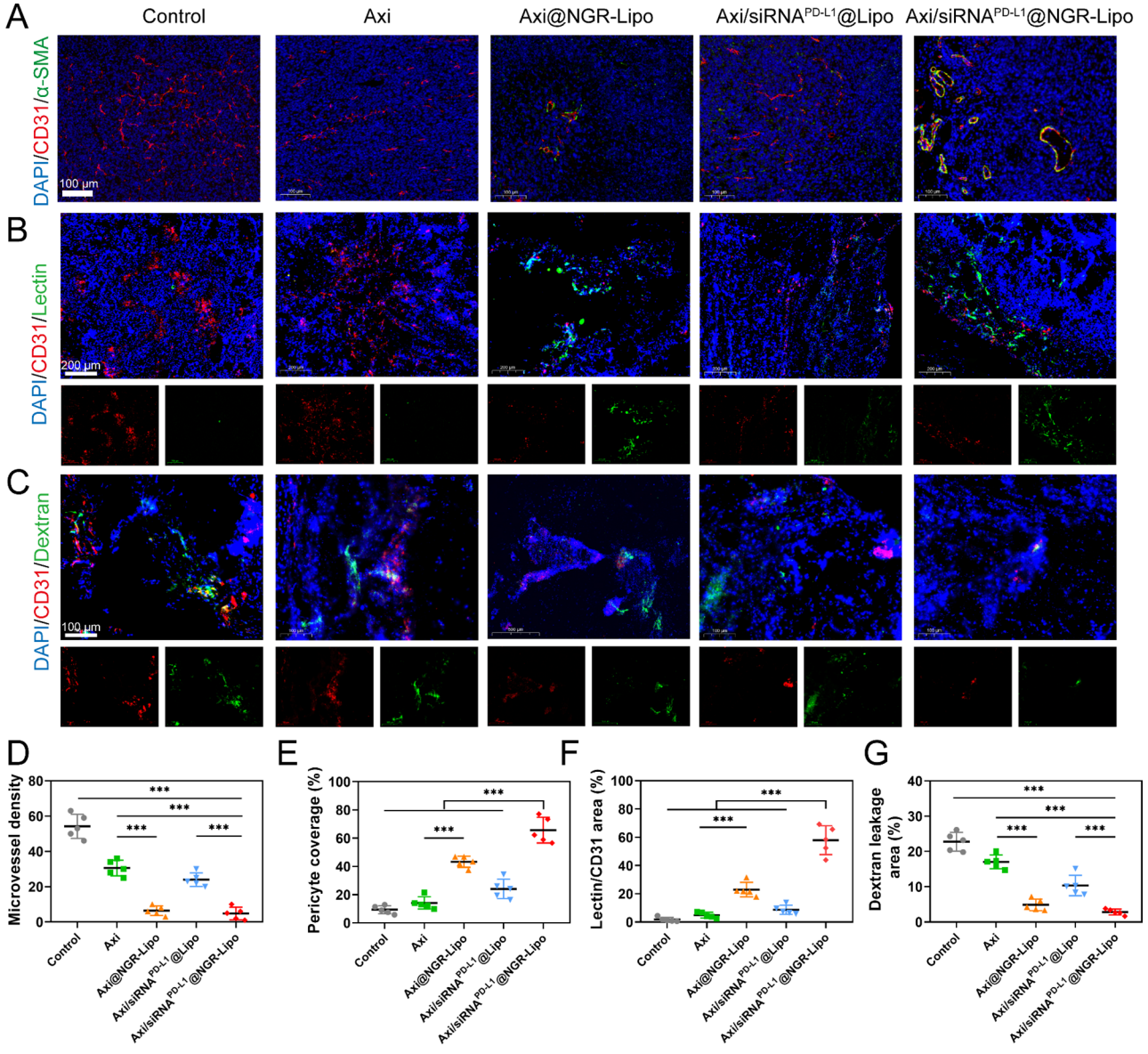

Fig. 8 Tumor vascular remodeling. (**A**) Representative images of tumor microvasculature (CD31, red) and pericytes (α-SMA, green) after various treatments. (**B**) Representative images of tumor vascular perfusion by FITC-lectin (green) after various treatments. (**C**) Representative images of tumor vascular permeability by FITC-dextran (green) after various treatments. (**D**) Microvessel density in the tumors after various treatments. Microvessel density was estimated by calculating the number of $CD31^+$ vessels on five fields from the tumor sections. (**E**) Pericyte coverage in the tumors after various treatments. Pericyte coverage was estimated by calculating α-SMA area (green) in a percent per total area on five fields from the tumor sections. (**F**) Quantitative analysis of tumor vascular perfusion areas after various treatments. The tumor vascular perfusion area was estimated by calculating $lectin^+$ area (green) in a percent per $CD31^+$ area (red) on five fields from the tumor sections. (**G**) Quantitative analysis of tumor vascular permeability areas after various treatments. The tumor vascular leakage area was estimated by calculating $dextran^+$ area (green) in a percent per total area on five fields from the tumor sections. Data were present as mean ± SD. ***$p < 0.001$

Afterward, to further validate the improvement of vascular function, vascular perfusion was assessed by intravenous injection of FITC-labelled lectin [38]. After treatment, FITC-labelled lectin was injected into the mice through the tail vein and the tumor was harvested after ten minutes. Compared with Control group, the fluorescence signal of FITC-labelled lectin (green fluorescence) was significantly increased in tumors in Axi/siRNA^{PD-L1}@NGR-Lipo group (Fig. 8B), suggesting higher vascular perfusion, and Axi/siRNA^{PD-L1}@NGR-Lipo improved vascular perfusion by 31.50-fold over the Control group (Fig. 8F). Furthermore, the improvement in vascular structural integrity was explored by injecting 70-kDa FITC-labelled dextran into the mice by tail vein after treatment. Tumor sections of Control group presented abundant leaking FITC-labelled dextran (green

fluorescence), while in the Axi/siRNA^{PD-L1}@NGR-Lipo group, little leaking dextran was detected, indicating reduced vascular permeability (Fig. 8C). Meanwhile, Axi/siRNA^{PD-L1}@NGR-Lipo treatment decreased vascular permeability by 87.56% over the Control group (Fig. 8G), implying a remarkable improvement of vascular structural integrity. These studies indicated that Axi/siRNA^{PD-L1}@NGR-Lipo could effectively improve vascular perfusion and decrease vascular permeability after normalizing the tumor vasculature, which would provide a favorable factor for enhancing the infiltration of immune cells into tumor tissue.

Mechanisms of immunotherapy in vivo

We initially elucidated the factors accounting for the excellent anti-tumor efficacy of Axi/siRNA^{PD-L1}@NGR-Lipo in terms of tumor vascular remodeling, and then attempted to proceed with the elucidation from the perspective of immune activation in vivo. It has been proposed that anti-angiogenic therapy can induce systemic immune modulation, with downregulation of myeloid-derived suppressor (MDSC) cells and regulatory T cells (Tregs), as well as the significant increase of cytotoxic T cells expressing PD-1 and natural killer (NK) cells [39]. Therefore, we investigated the proportion of different immune-associated cells in tumors by flow cytometry analysis of the tumor tissues after various treatments. Cytotoxic T lymphocytes (CTL, $CD8^+$) are the main force of the anti-tumor immune response and play a role in killing tumor cells. As expected, Axi/siRNA^{PD-L1}@NGR-Lipo significantly increased the infiltration of $CD8^+$ T cells ($CD45^+CD3^+CD8^+$) in the tumor (Fig. 9A), with about 5.04-fold higher than the Control group (Fig. 9B). Similar results were also revealed in immunofluorescence, where more red fluorescent signals of $CD8^+$ T cells were presented in tumors of Axi/siRNA^{PD-L1}@NGR-Lipo (Fig. 9J and Fig. S11). In addition, NK cells exercise an immune surveillance function in the body and are also the backbone of eliminating tumor cells. Flow cytometry analysis revealed that Axi/siRNA^{PD-L1}@NGR-Lipo significantly increased the proportion of NK cells ($CD45^+CD3^-CD49b^+$) in tumors by 1.69-fold over the Control group (Fig. 9C and D). The substantially higher proportion of $CD8^+$ T cells and NK cells infiltrating the tumor could support the excellent anti-tumor effect of Axi/siRNA^{PD-L1}@NGR-Lipo.

Nevertheless, immunosuppressive cells, including Tregs and MDSCs, would significantly inhibit the activation of $CD8^+$ T cells and impede the anti-tumor immune response [40]. Next, we examined the proportion of Tregs and MDSCs within the tumor by flow cytometry assay. Encouragingly, Axi/siRNA^{PD-L1}@NGR-Lipo significantly reduced the proportion of infiltrating Tregs ($CD45^+CD3^+CD4^+CD25^+FOXP3^+$) to 5.97% compared to the Control group with the Tregs infiltration of 33.1% (Fig. 9E and F). Similarly, Axi/siRNA^{PD-L1}@NGR-Lipo brought down the proportion of MDSCs ($CD45^+CD11c^+CD11b^+Gr\text{-}1^+$) within the tumor considerably, with only 8.22% compared to 33.9% in the Control group (Fig. 9G and H). Immunofluorescence also showed a familiar trend, with the green fluorescent signals of $FOXP3^+$ Tregs (Fig. 9K and Fig. S12) and $CD11b^+$ MDSCs (Fig. 9L and Fig. S13) almost invisible in the Axi/siRNA^{PD-L1}@NGR-Lipo group. Therefore, we consider that the immunosuppressive microenvironment of tumors could be effectively reversed by Axi/siRNA^{PD-L1}@NGR-Lipo.

Although $CD8^+$ T cells infiltrated within the tumor were greatly increased, high expression of PD-L1 protein on the surface of the tumor cells prevented $CD8^+$ T cells from recognizing tumor cells, resulting in immune evasion and reduced anti-tumor efficacy. Additionally, in vitro cellular experiments have demonstrated that the treatment with Axi alone caused elevated PD-L1 protein expression on the surface of tumor cells, which exacerbated the immune evasion of tumor cells. However, it has been reported that the increasing tumor PD-L1 expression could potentially sensitize tumors to ICI therapies. Subsequently, we performed immunohistochemistry (IHC) to examine the silencing efficiency of PD-L1 protein in vivo experiments. As shown in Fig. 9I and Fig. S14, Axi/siRNA^{PD-L1}@NGR-Lipo could effectively silence the PD-L1 genes and decrease the expression of PD-L1 proteins. As a result, Axi/siRNA^{PD-L1}@NGR-Lipo not only effectively exerts anti-tumor effects, but also reduces the side effects of elevated PD-L1 protein caused by Axi alone, achieving a match made in heaven between the two agents.

Transcriptome sequencing analysis

To further explore the molecular mechanisms of remodeling the tumor vascular system and immunotherapy, we performed transcriptome sequencing analysis of tumors from Control and Axi/siRNA^{PD-L1}@NGR-Lipo groups. As shown in the volcano plot (Fig. 10A), 237 differential genes were detected after Axi/siRNA^{PD-L1}@NGR-Lipo treatment compared with Control, with 107 up-regulated genes (red dots) and 130 down-regulated genes (blue dots). Venn diagram illustrates the amount of all genes detected in Control group and Axi/siRNA^{PD-L1}@NGR-Lipo group (Fig. 10B). Gene ontology (GO) enrichment analysis showed that after Axi/siRNA^{PD-L1}@NGR-Lipo treatment, differential genes were mainly enriched in immune response and tumor vascular system-related pathways (Fig. 10C). Immune response-related signaling pathways were significantly upregulated after Axi/siRNA^{PD-L1}@NGR-Lipo treatment, including NK cytokine production and mediated immune, innate and adaptive immune response, cell killing and T cell differentiation.

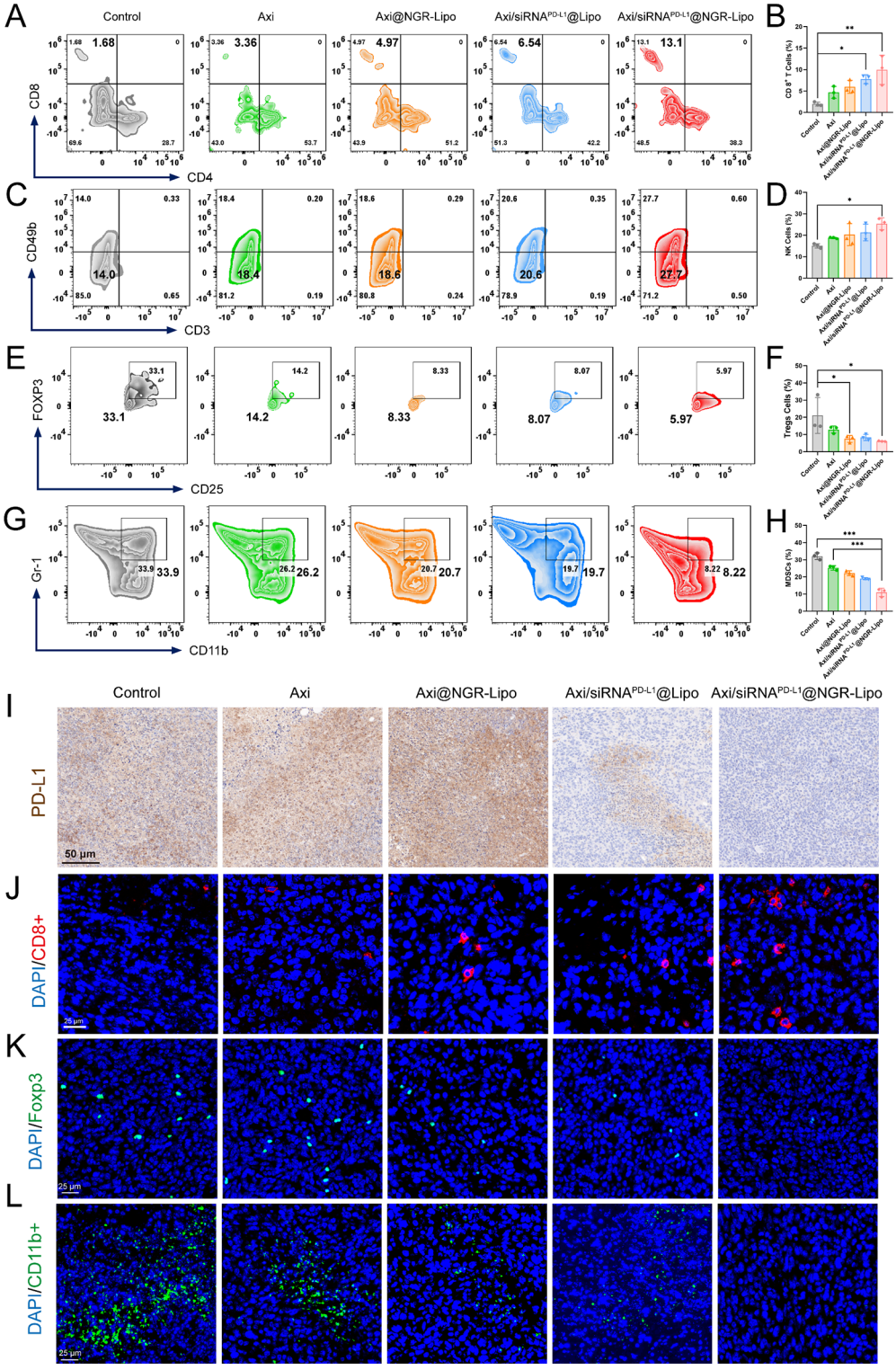

Fig. 9 Immune activation in vivo. (**A**) Flow cytometry assay and (**B**) quantitative analysis of CD8$^+$ T cells (CD45$^+$CD3$^+$CD8$^+$) infiltrated in tumors after various treatments ($n = 3$). (**C**) Flow cytometry assay and (**D**) quantitative analysis of NK cells (CD45$^+$CD3$^-$CD49b$^+$) in tumors after various treatments ($n = 3$). (**E**) Flow cytometry assay and (**F**) quantitative analysis of Tregs cells (CD45$^+$CD3$^+$CD4$^+$CD25$^+$FOXP3$^+$) in tumors after various treatments ($n = 3$). (**G**) Flow cytometry assay and (**H**) quantitative analysis of MDSCs (CD45$^+$CD11c$^+$CD11b$^+$Gr-1$^+$) in tumors after various treatments ($n = 3$). (**I**) Immunohistochemistry of PD-L1 protein on tumors after various treatments. (**J**) Immunofluorescence of CD8$^+$ T cells (Red) in tumors after various treatments. (**K**) Immunofluorescence of Tregs cells (FOXP3$^+$: green) in tumors after various treatments. (**L**) Immunofluorescence of MDSCs (CD11b$^+$: green) in tumors after various treatments. Data were present as mean ± SD. *$p < 0.05$, **$p < 0.01$, ***$p < 0.001$

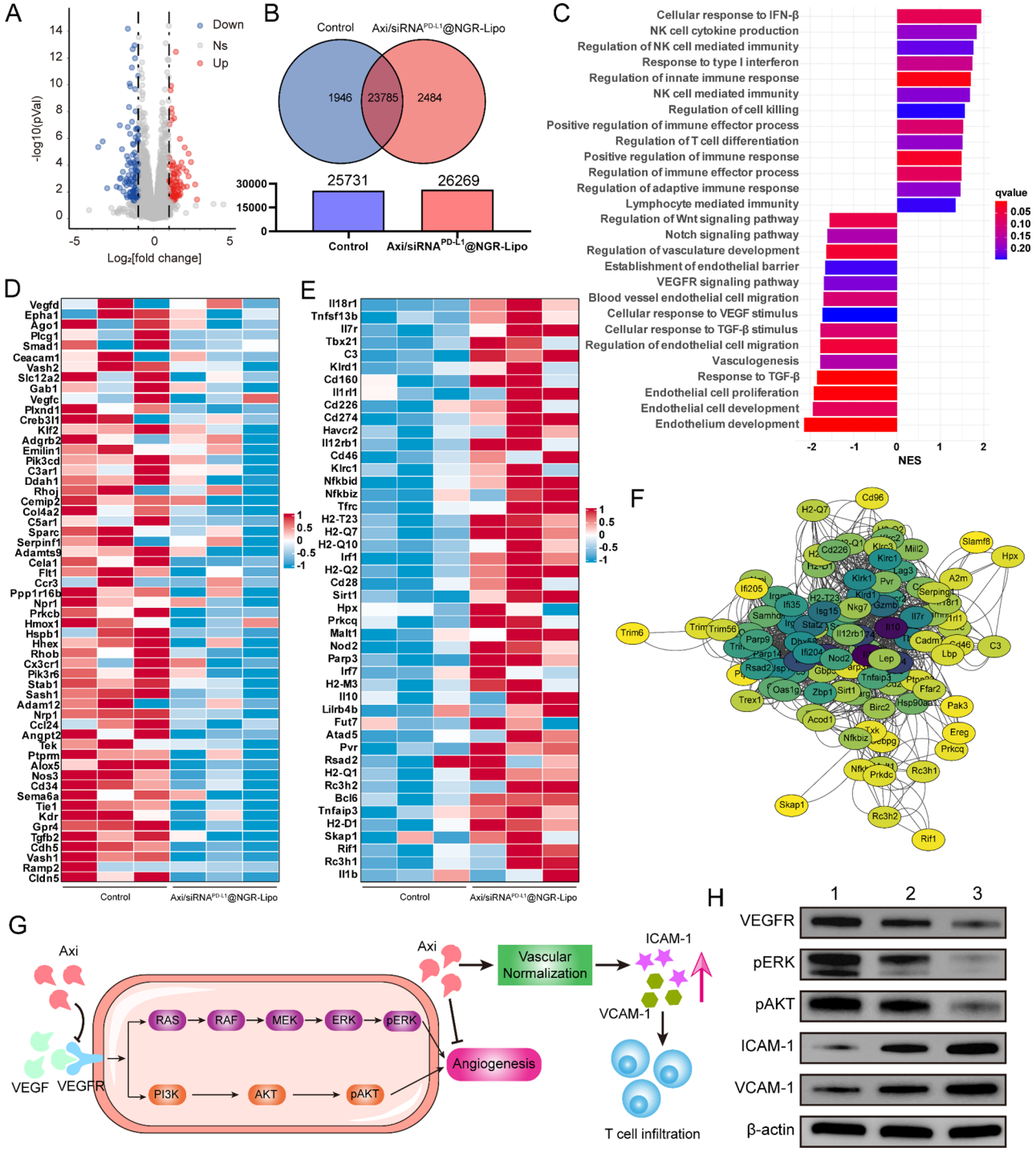

Fig. 10 Transcriptome sequencing analysis. (**A**) Volcano plots of the total differentially expressed genes between Control and Axi/siRNA^{PD-L1}@NGR-Lipo group. (**B**) Venn diagram of all expressed genes. (**C**) GO enrichment after Axi/siRNA^{PD-L1}@NGR-Lipo treatment. Heatmap analysis of gene expression involved in vasculature development (**D**) and adaptive immune response (**E**). (**F**) Protein–protein interaction network. (**G**) The mechanism illustration of Axi/siRNA^{PD-L1}@NGR-Lipo facilitating T cell infiltration through inhibition of angiogenesis. (**H**) Western blot analysis of VEGFR, pERK, pAKT, ICAM-1 and VCAM-1 proteins in mouse tumors after different treatments. 1: Control 2: Axi 3: Axi/siRNA^{PD-L1}@NGR-Lipo

In contrast, angiogenesis-related signaling pathways were significantly downregulated, including vasculature development, vascular endothelial cell growth factor stimulus, and endothelial cell proliferation and development. Subsequently, we analyzed the expression levels of genes associated with the angiogenic system and found that genes related to vasculature development (Fig. 10D), blood vessel endothelial cell migration (Fig. S15),

endothelial cell proliferation (Fig. S16), and establishment of endothelial barriers (Fig. S17) were all significantly downregulated in Axi/siRNA^{PD-L1}@NGR-Lipo group. On the contrary, heat maps show that gene expression levels of immune-related signaling pathways in Axi/siRNA^{PD-L1}@NGR-Lipo group displayed an elevated trend, including adaptive immune response (Fig. 10E), innate immune response (Fig. S18), NK cell-mediated immunity (Fig. S19), T cell differentiation (Fig. S20) and regulation of immune response processes (Fig. S21). Meanwhile, Protein-protein interaction (PPI) network indicated that genes of angiogenesis-related pathways and immunity-related pathways were closely associated with each other (Fig. 10F).

To validate the therapeutic mechanism of Axi/siRNA^{PD-L1}@NGR-Lipo, we further explored the downstream signaling pathways. As shown in Fig. 10G, the binding of VEGF to the VEGF receptor (VEGFR) could activate RAS/RAF/MEK/ERK signaling pathway and PI3K/AKT signaling pathway, consequently promoting neoangiogenesis. Axitinib, as a multi-targeted tyrosine kinase inhibitor, can efficiently and selectively inhibit the activity of VEGFR. The results of western blot analysis (Fig. 10H) clearly demonstrated that after treatment with Axi/siRNA^{PD-L1}@NGR-Lipo, the expression of VEGFR protein in mouse tumors was significantly reduced. Simultaneously, the downregulated expression of pERK and pAKT proteins provided compelling evidence for the inhibition of RAS/RAF/MEK/ERK and PI3K/AKT signaling pathways. Upon inhibiting the activity of VEGFR and subsequent blocking of the downstream pathway, Axi/siRNA^{PD-L1}@NGR-Lipo could normalize the tumor vascular structure, thereby leading to an improvement in vascular perfusion and permeability. The normalized vascular endothelial cells expressed certain specific adhesion molecules and chemokines, including ICAM-1 and VCAM-1, as shown in Fig. 10H. These molecules played a crucial role in guiding T cells to migrate from the circulation and adhere to the tumor vascular endothelium through binding to the receptors on T cell surface, subsequently facilitating the infiltration of T cells into the tumor tissue. In summary, transcriptome sequencing and western blot analysis further confirmed the positive role of Axi/siRNA^{PD-L1}@NGR-Lipo in inhibiting tumor angiogenesis and remodeling the vascular system, thereby promoting T and NK cell infiltration, initiating innate and adaptive immunity, and potentiating anti-tumor immunotherapeutic efficacy.

Conclusion

In conclusion, we successfully constructed NGR peptide-modified actively targeted liposomes for co-encapsulating the anti-angiogenic drugs Axi and PD-L1 siRNA. This well-designed Axi/siRNA^{PD-L1}@NGR-Lipo liposome remarkably inhibited the generation of microvessels in tumor tissues, increased the percentage of pericyte coverage, and normalized the structure and function of the tumor vascular system, which resulted in a striking increase of the infiltrating CTLs and NK cells proportion, thus obtaining surprising anti-tumor immune therapeutic effects. Meanwhile, the normalized tumor vasculature gave rise to a decrease of immunosuppressive cells including MDSCs and Tregs. Axi/siRNA^{PD-L1}@NGR-Lipo also effectively inhibited pulmonary metastases. We found that the co-loaded liposome system circumvented the risk of reduced immunotherapeutic efficacy arising from elevated PD-L1 protein on the surface of tumor cells caused by Axi. The novel liposomes proposed herein offer a promising paradigm for combining anti-angiogenic therapies and ICI in treating RCC and enhancing the immunotherapeutic efficacy of various solid tumors.

Materials and methods

Materials

Axitinib was brought from Shanghai Macklin Biochemical Co., Ltd. (Shanghai, China). PD-L1 siRNA was obtained from Suzhou GenePharma Co., Ltd. (Suzhou, China). NGR peptides (CYGGRGNG) were brought from DGpeptides Co., Ltd. (Wuhan, China). Protamine was purchased from Sigma Aldrich (Beijing, China). Cholesterol and 1,2-dioleoyl-sn-glycero-3-phosphocholine (DOPC) were bought from AVT Shanghai Pharmaceutical Tech Co., Ltd (Shanghai, China). DSPE-PEG2000-Mal was purchased from Aladdin Biochemical Technology Co., Ltd. (Shanghai, China). Coumarin-6 (Cou-6) was obtained from J&K Scientific Co., Ltd. (Beijing, China). Lectin, FITC-dextran and 4′,6-diamidino-2-phenylindole (DAPI) were brought from Solarbio Life Sciences Co., Ltd. (Beijing, China). The Annexin V-FITC Apoptosis Kit (K2003) was brought from APExBIO (Houston, USA). Cell-Counting Kit-8 (CCK-8) was brought from Dojindo Laboratories (Kumamoto, Japan). Calcein-AM and propidium iodide (PI) were brought from Shanghai Beyotime Biotechnology Inc. (Shanghai, China). Anti-PD-L1 antibodies were purchased from Wuhan Servicebio Technology Co., Ltd (Wuhan, China). FITC-anti-CD45, anti-CD3, anti-CD4, anti-CD8, PE-anti-CD49b, anti-CD11b, anti-Ly-6G/Ly-6 C (Gr-1), APC anti-CD25 and PE anti-FOXP3 antibodies were brought from Biolegend. Anti-α-SMA (Ab124964) and anti-CD31 antibodies were brought from Abcam Ltd. (Cambridge, UK).

Synthesis of DSPE-PEG2000-NGR

The synthesis of DSPE-PEG2000-NGR was carried out according to previous research with slight modifications [41]. Briefly, 50 mg of NGR peptides and 154 mg of DSPE-PEG2000-MAL were fully dissolved in 10 mL of HEPEs solution (pH 8.0) and stirred at room temperature

for 24 h in N_2 atmosphere for protection. After the reaction, free peptides were removed using the dialysis bag (MWCO 2500) and the final product was obtained by lyophilization. The structure and molecular weight of DSPE-PEG2000-NGR were corroborated by ^{1}H NMR spectroscopy and MALDI-TOF MS, respectively.

Preparation and characterization of Axi/siRNA^{PD-L1}@NGR-Lipo

Firstly, Pro-siRNA^{PD-L1} was prepared by the charge interaction of protamine with siRNA^{PD-L1}. In brief, protamine and siRNA^{PD-L1} were mixed in the same volume with different mass ratios (5:1, 4:1, 3:1, 2:1, 1:1) and vortexed for 5 min. Pro-siRNA^{PD-L1} was obtained after incubation. Subsequently, Axi/siRNA^{PD-L1}@NGR-Lipo was prepared by film dispersion method. In particular, 1 mg Axitinib was fully dissolved in methanol and then added to the methylene chloride solution containing 4 mg cholesterol, 20 mg DOPC and 4 mg DSPE-PEG2000-NGR. The mixture was passed through a rotary evaporator to form a phospholipid film at 40 °C under reduced pressure and remove the residual organic solvent. Subsequently, the phospholipid films were hydrated with water at 40 °C for 30 min. Axi@NGR-Lipo was obtained after sonication in ice water at 60 W for 20 min under probe sonication. Afterward, Pro-siRNA^{PD-L1} was thoroughly mixed with Axi@NGR-Lipo. Axi/siRNA^{PD-L1}@NGR-Lipo was obtained by extruding 20 times through a 0.22 μm polycarbonate membrane filters using a lipid extruder (Avanti Polar Lipids). The preparation procedure of Axi/siRNA^{PD-L1}@Lipo was similar to that described above, except that DSPE-PEG2000-NGR was replaced with DSPE-PEG2000.

The particle size distribution and surface zeta potential of Pro-siRNA^{PD-L1}, Axi/siRNA^{PD-L1}@Lipo and Axi/siRNA^{PD-L1}@NGR-Lipo were determined by dynamic light scattering analyzer (DLS, Zetasizer Nano ZS90; Malvern Instruments Ltd., UK). The morphology of Pro-siRNA^{PD-L1}, Axi/siRNA^{PD-L1}@Lipo and Axi/siRNA^{PD-L1}@NGR-Lipo were characterized with transmission electron microscopy (JEM-1400PLUS; JEOL Ltd., Tokyo, Japan). The colloidal stability of Axi/siRNA^{PD-L1}@NGR-Lipo was investigated by measuring the change of particle size in water, PBS, RPMI-1640 and 5% glucose.

Agarose gel retardation assay

The encapsulation of Pro-siRNA^{PD-L1} complexes formed by different mass ratios of protamine and siRNA^{PD-L1} (5:1, 4:1, 3:1, 2:1, 1:1) was evaluated by 1% agarose gel electrophoresis. Specifically, the Pro-siRNA^{PD-L1} complexes was incorporated into the agarose gel according to the protocol, separated in an electrophoresis apparatus at 120 V for 10 min, and then photographed in a UV imager.

Cell culture

Mouse renal cancer cells (Renca cells) and human umbilical vein endothelial cells (HUVEC cells) were acquired from the Cell Culture Center of the Institute of Basic Medical Sciences at the Chinese Academy of Medical Sciences (CAMS, China). Renca cells were cultured with 1640 complete medium containing 10% fetal bovine serum (FBS), 1% penicillin and streptomycin, and 1% glutamine in an incubator at 37 °C and 5% CO_2. HUVEC cells were cultured with DMEM complete medium containing 10% fetal bovine serum (FBS), 1% penicillin and streptomycin, and 1% glutamine in an incubator at 37 °C and 5% CO_2. All experiments were conducted when the cells were in the logarithmic growth phase.

Cellular uptake assay

For more visual observation, Cou-6 was employed instead of Axi to investigate the uptake of liposomes by HUVEC cells and Renca cells, respectively. In detail, HUVEC cells or Renca cells were seeded in 12-well plates (20×10^4 cells per well) pre-positioned with cell crawlers. After incubation overnight, cells were divided into 5 groups and given various preparations: free Cou-6, Cou-6@Lipo, Cou-6@Lipo + NGR, Cou-6@NGR-Lipo, Cou-6@NGR-Lipo + NGR, at an equivalent Cou-6 concentration of 5 μg/mL, where Cou-6@Lipo + NGR and Cou-6@NGR-Lipo + NGR groups were supplemented in advance with an excess of free NGR peptide (1 mg/mL) to saturate the receptor. After incubation for 4 h, cells were fixed with paraformaldehyde and nuclei were stained with DAPI. The cellular uptake of liposomes was observed by a confocal laser scanning microscopy (CLSM, TCS SP2; Leica, Germany). For quantitative analysis, flow cytometry (FCM, Becton Dickinson, Franklin Lake, NJ, USA) was employed to investigate the efficiency of liposome uptake by HUVEC cells and Renca cells.

Western blot

Western blot was performed to examine the effect of Axi on the expression of PD-L1 protein on the surface of Renca cells. In short, Renca cells were seeded in 6-well plates (30×10^4 cells/well) and incubated with Control, Axi (0.4 μg/mL) and Axi (4 μg/mL) for 24 h, respectively. Cells are lysed with a cocktail of protease inhibitors and RIPA solution for 30 min on ice. The protein concentration of the supernatant was determined using the BCA Protein Concentration Assay Kit. After separation by SDS-PAGE electrophoresis, proteins were transferred to a 0.45 μm PVDF membrane. The PVDF membrane was incubated with the primary antibody on a shaker at 4°C overnight after blocking. Then, the membrane was incubated with the secondary antibody and blotted with Enhanced Chemiluminescence (ECL) luminescent solution to be imaged in an ECL system. Furthermore, the

efficiency of silencing of PD-L1 protein on the surface of Renca cells by various preparations in vitro was assessed. In particular, Renca cells were seeded in 6-well plates (30×10^4 cells/well) and incubated with Control, Axi, siRNA^{PD-L1}, Axi/siRNA^{PD-L1}@Lipo and Axi/siRNA^{PD-L1}@NGR-Lipo (siRNA^{PD-L1}: 100nM) for 24 h, respectively. Subsequent imaging of the PD-L1 protein was performed following similar procedures as above.

Cell viability assay

The inhibition of proliferation of Renca cells and HUVEC cells by various preparations was studied using CCK-8 assays. In brief, Renca cells or HUVEC cells were seeded in 96-well plates (5000 cells/well) and incubated for 24 h. Then, the medium containing different concentrations of free Axi, Axi/siRNA^{PD-L1}@Lipo and Axi/siRNA^{PD-L1}@NGR-Lipo were added, with the concentrations ranging from 2.5 μg/mL, 5 μg/mL, 10 μg/mL, 20 μg/mL, 40 μg/mL, 60 μg/mL and 80 μg/mL. After continuing culturing for 24 h, each well was supplemented with 100 μL of serum-free medium containing CCK-8 (0.5 mg/mL). The absorbance value at 450 nm was measured using a microplate reader (BioTek, Dallas, TX, USA). Cell viability was calculated by the following formula.

$$\text{Cell viability } (\%) = \frac{\text{OD}_{\text{test}} - \text{OD}_{\text{blank}}}{\text{OD}_{\text{control}} - \text{OD}_{\text{blank}}} \times 100\%$$

Cell apoptosis assay

The apoptosis induced by various preparations on Renca cells and HUVEC cells was assayed by Annexin V-FITC/PI staining method. Renca cells or HUVEC cells were inoculated in 6-well plates (30×10^4 cells/well) and cultured for 24 h. Then, the cells were treated with free Axi, Axi/siRNA^{PD-L1}@Lipo and Axi/siRNA^{PD-L1}@NGR-Lipo, where the concentration of Axi was 30 μg/mL. After incubating for 24 h, cell suspensions were collected and stained with FITC and PI for 15 min, respectively. The percentage of apoptosis was detected and analyzed by a FACSCalibur flow cytometry (Becton Dickinson, Franklin Lakes, NJ, USA).

Live/dead cell staining

Calcein-AM and Propidium Iodide (PI) kits were applied to investigate the live/dead cell staining of Renca and HUVEC cells by different preparations. Renca cells or HUVEC cells were inoculated in 12-well plates (20×10^4 cells/well) and treated with free Axi, Axi/siRNA^{PD-L1}@Lipo and Axi/siRNA^{PD-L1}@NGR-Lipo (Axi: 20 μg/mL) for 12 h. Subsequently, the samples were stained with Calcein-AM and PI for 30 min and then the fluorescence of live and dead cells was observed under an inverted fluorescence microscope.

In vitro penetration and growth inhibition assays of tumor spheres

In vitro 3D tumor sphere models were constructed to investigate the penetration and growth inhibition of tumors by various agents [42]. To construct 3D tumor spheres, 100 μL of suspension containing Renca cells was added to a 96-well plate covered with a 1.5% (weight/volume) agarose gel. When the tumor spheres grew to about 300 μm of diameter, free Cou-6, Cou-6@Lipo and Cou-6@NGR-Lipo (Cou-6: 5 μg/mL) were added, respectively. After 12 h of incubation, the tumor spheres were removed and placed in confocal dishes to observe the penetration under CLSM, where images were captured tomographically from the top of the spheres every 10 μm.

In the assay investigating the growth inhibition of tumor spheres by liposomes, 3D tumor spheres were constructed in accordance with the above method. Subsequently, free Axi, Axi/siRNA^{PD-L1}@Lipo and Axi/siRNA^{PD-L1}@NGR-Lipo (Axi: 30 μg/mL) were added and untreated wells were set up as Control group. The growth and images of tumor spheres were observed and recorded every two days over a period of 7 days using a microscope.

Establishment of subcutaneous renal tumor model

The subcutaneous renal tumor models were constructed by injection of 200 μL of suspension containing 1×10^6 Renca cells subcutaneously into the left intercostal space of male BALB/c mice (6–8 weeks old). The mice were brought from Gempharmatech Co., Ltd (Beijing, China). All animal experiments were performed under the guidance of the Laboratory Animal Ethics Committee of the Institute of Materia Medica in CAMS and PUMC.

Biodistribution of liposomes in vivo

The biodistribution of liposomes in mice was investigated by an in vivo imaging system. In order to observe the distribution of liposomes in different tissues visually, DiR was encapsulated in liposomes instead of Axi and prepared in a similar way. Mice ($n=3$) bearing subcutaneous renal tumors were intravenously injected with free DiR, DiR@Lipo and DiR@NGR-Lipo (0.25 mg/kg) when the tumor volume reached 300 mm^3. The distribution of fluorescent signals in vivo was observed by an in vivo imaging system (IVIS, Caliper Life Sciences Inc., Mountain View, CA, USA) at the scheduled time point after injection. At 24 h post-injection, major organs of mice, including heart, liver, spleen, lungs and kidneys, as well as tumors, were dissected and removed to detect the ex vivo fluorescence signals of different tissues. Finally, the fluorescence signal intensity was quantitatively analyzed using in vivo imaging software (version 4.3.1; Caliper Life Sciences Inc.).

Evaluation of anti-tumor activity in subcutaneous renal tumor model

After subcutaneous implantation of Renca cells and 7 days of tumor growth, tumor-bearing mice were randomly divided into 5 groups and injected intravenously with saline, Axi, Axi@NGR-Lipo, Axi/siRNA^{PD-L1}@Lipo and Axi/siRNA^{PD-L1}@NGR-Lipo (Axi: 25 mg/kg, siRNA: 1 mg/kg), respectively, for 5 consecutive injections every three days. During the treatments, body weights and tumor volumes of the mice were measured and recorded. On the third day after the last administration, mice were dissected and major organs, including heart, liver, spleen, lungs and kidneys, were removed for hematoxylin and eosin (HE) staining. The removed tumors were photographed and weighed and sectioned for terminal deoxynucleotidyltransferase mediated nick end labeling (TUNEL) staining and HE staining. Mice serum samples were collected for ALT, AST, BUN and CRE assays. Moreover, other tumor-bearing mice were treated by injecting various agents ($n = 10$) and the survival of the mice was monitored and survival curves were plotted.

Tumor vascular remodeling in vivo

Three days after the last treatment, the mouse tumors were removed for sectioning and staining. The vascular function was assessed by immunohistochemical (IHC) staining of pericytes using α-SMA (1:100) and vascular morphology was assessed by IHC staining tumor vessels with CD31, according to the manufacturer's instructions.

On the third day after the above treatment, mice with Renca cells were studied for vascular perfusion function by intravenous injection of FITC-labelled lectin (100 μL 1 mg/mL). Ten minutes post-injection, mice tumors were collected for frozen sections. Tumor blood vessels were stained with anti-CD31 antibody and nuclei were stained with DAPI. The area of perfusion was determined by calculating the area of the lectin in percentage of the area of CD31.

On the third day after the above treatment, mice bearing Renca cells were studied for vascular leakage by intravenous injection of FITC-labelled dextran (70 kDa, 100 μL 20 mg/mL). Half an hour after injection, mice tumors were collected for frozen sections. Tumor blood vessels were stained with anti-CD31 antibody and nuclei were stained with DAPI. The leakage area within the tumor was estimated by calculating the area of FITC-dextran in a percent per total area.

Mechanisms of the in vivo immunotherapy

To investigate the mechanism of immunotherapy in vivo, mice bearing tumors were treated according to the above treatment protocol. On the third day after treatment, the tumors of the mice were removed for flow analysis. The proportion of $CD4^+$ T cells and $CD8^+$ T cells infiltrated in the tumors was determined by staining with FITC-anti-CD45, anti-CD3, anti-CD4, and anti-CD8 antibodies, respectively. The proportion of Tregs cells in the tumor was determined by FITC-anti-CD45, anti-CD3, anti-CD4, APC anti-CD25 and PE-anti-FOXP3 antibodies. To investigate the infiltrated NK cells in the tumor, FITC-anti-CD45, anti-CD3 and PE-anti-CD49b were taken for staining. Also, MDSCs cells in tumors were detected by staining with FITC-anti-CD45, anti-CD11b and anti-Ly-6G/Ly-6 C (Gr-1) antibodies. Finally, all samples were analyzed by flow cytometry. Furthermore, the expression of PD-L1 protein on the surface of tumor cells was detected by immunohistochemistry. $CD8^+$ T cells, Tregs cells and MDSCs cells in tumor tissues were also visualized by immunofluorescence staining for CD8, FOXP3 and CD11b.

Transcriptome sequencing analysis

After treatment with saline and Axi/siRNA^{PD-L1}@NGR-Lipo, tumors were collected for RNA sequencing analysis on Illumina NovaSeq 6000 platform. Differentially expressed genes (DEGs) were screened using DESeq2 software, with Log2(Fold Change) ≥ 1 and FDR < 0.05 as the screening criteria.

Statistical analysis

All results are expressed as mean ± standard deviation (SD). Data analysis between different groups was performed by one-way ANOVA. Statistical significance between groups was expressed by $^*P < 0.05$, $^{**}P < 0.01$, $^{***}P < 0.001$.

Supplementary Information

The online version contains supplementary material available at https://doi.org/10.1186/s12951-025-03170-y.

Supplementary Material 1

Acknowledgements

Not applicable.

Author contributions

Yanhong Liu and Liming Gong have made substantial contributions to the conception, design of the work, the acquisition, analysis, interpretation of data and have drafted the work and substantively revised it. Jing Feng, Congcong Xiao and Chenfei Liu did the work including preparation and characterization, agarose gel retardation assay. Bohan Chen andLiqing Chen did the work including in vivo anti-tumor efficacy and biosafety. Mingji Jin prepared Figs. 5, 6 and 7. Youyan Guan, Zhonggao Gao and Wei Huang have made substantial contributions to the conception.

Funding

This work was financially supported by CAMS Innovation Fund for Medical Sciences (CIFMS) (2021-I2M-1-026, China).

Data availability

No datasets were generated or analysed during the current study.

Declarations

Ethics approval and consent to participate
All animal experiments were conducted with the approval of the Laboratory Animal Ethics Committee of the Institute of Materia Medica in CAMS and PUMC.

Competing interests
The authors declare no competing interests.

Author details
[1]State Key Laboratory of Bioactive Substance and Function of Natural Medicines, Department of Pharmaceutics, Institute of Materia Medica, Chinese Academy of Medical Sciences and Peking Union Medical College, Beijing 100050, China
[2]Department of Urology, National Cancer Center/National Clinical Research Center for Cancer/Cancer Hospital, Chinese Academy of Medical Sciences and Peking Union Medical College, Beijing 100021, China
[3]Department of Pharmacy, Suzhou Municipal Hospital, The Affiliated Suzhou Hospital of Nanjing Medical University, Gusu School of Nanjing Medical University, Suzhou 215000, China
[4]Beijing Key Laboratory of Drug Delivery Technology and Novel Formulations, Institute of Materia Medica, Chinese Academy of Medical Sciences and Peking Union Medical College, Beijing 100050, China

Received: 26 November 2024 / Accepted: 27 January 2025
Published online: 10 March 2025

References

1. Rini BI, Campbell SC, Escudier B. Renal cell carcinoma. Lancet. 2009;373:1119–32.
2. Sung H, Ferlay J, Siegel RL, Laversanne M, Soerjomataram I, Jemal A, Bray F. Global cancer statistics 2020: GLOBOCAN estimates of incidence and mortality worldwide for 36 cancers in 185 countries. CA Cancer J Clin. 2021;71:209–49.
3. Hsieh JJ, Purdue MP, Signoretti S, Swanton C, Albiges L, Schmidinger M, Heng DY, Larkin J, Ficarra V. Renal cell carcinoma. Nat Reviews Disease Primers. 2017;3:17009.
4. Atkins MB, Tannir NM. Current and emerging therapies for first-line treatment of metastatic clear cell renal cell carcinoma. Cancer Treat Rev. 2018;70:127–37.
5. Siegel RL, Miller KD, Fuchs HE, Jemal A. Cancer statistics, 2021. CA Cancer J Clin. 2021;71:7–33.
6. Patel HV, Shinder B, Srinivasan R, Singer EA. Challenges and opportunities in the management of metastatic renal cell carcinoma: combination therapy and the role of cytoreductive surgery. Curr Opin Oncol. 2020;32:240–9.
7. Huinen ZR, Huijbers EJM, van Beijnum JR, Nowak-Sliwinska P, Griffioen AW. Anti-angiogenic agents - overcoming tumour endothelial cell anergy and improving immunotherapy outcomes. Nat Reviews Clin Oncol. 2021;18:527–40.
8. Li TS, Xu LJ, Wei Z, Zhang SM, Liu XY, Yang YZ, Gu Y, Zhang J. ELF5 drives angiogenesis suppression though stabilizing WDTC1 in renal cell carcinoma. Mol Cancer. 2023;22:184.
9. Munn LL, Jain RK. Vascular regulation of antitumor immunity. Science. 2019;365:544–5.
10. Cao Y, E G, Wang E, Pal K, Dutta SK, Bar-Sagi D, Mukhopadhyay D. VEGF exerts an angiogenesis-independent function in Cancer cells to promote their malignant progression. Cancer Res. 2012;72:3912–8.
11. Huang Y, Kim BYS, Chan CK, Hahn SM, Weissman IL, Jiang W. Improving immune–vascular crosstalk for cancer immunotherapy. Nat Rev Immunol. 2018;18:195–203.
12. De Palma M, Biziato D, Petrova TV. Microenvironmental regulation of tumour angiogenesis. Nat Rev Cancer. 2017;17:457–74.
13. Chouaib S, Noman MZ, Kosmatopoulos K, Curran MA. Hypoxic stress: obstacles and opportunities for innovative immunotherapy of cancer. Oncogene. 2016;36:439–45.
14. Teng MWL, Ngiow SF, Ribas A, Smyth MJ. Classifying cancers based on T-cell infiltration and PD-L1. Cancer Res. 2015;75:2139–45.
15. Ronca R, Benkheil M, Mitola S, Struyf S, Liekens S. Tumor angiogenesis revisited: regulators and clinical implications. Med Res Rev. 2017;37:1231–74.
16. Hicklin DJ, Ellis LM. Role of the vascular endothelial growth factor pathway in Tumor Growth and Angiogenesis. J Clin Oncol. 2005;23:1011–27.
17. Gabrilovich DI, Chen HL, Girgis KR, Cunningham HT, Meny GM, Nadaf S, Kavanaugh D, Carbone DP. Production of vascular endothelial growth factor by human tumors inhibits the functional maturation of dendritic cells. Nat Med. 1996;2:1096–103.
18. Terme M, Pernot S, Marcheteau E, Sandoval F, Benhamouda N, Colussi O, Dubreuil O, Carpentier AF, Tartour E, Taieb J. VEGFA-VEGFR pathway blockade inhibits Tumor-Induced Regulatory T-cell proliferation in Colorectal Cancer. Cancer Res. 2013;73:539–49.
19. Gavalas NG, Tsiatas M, Tsitsilonis O, Politi E, Ioannou K, Ziogas AC, Rodolakis A, Vlahos G, Thomakos N, Haidopoulos D, et al. VEGF directly suppresses activation of T cells from ascites secondary to ovarian cancer via VEGF receptor type 2. Br J Cancer. 2012;107:1869–75.
20. Voron T, Colussi O, Marcheteau E, Pernot S, Nizard M, Pointet A-L, Latreche S, Bergaya S, Benhamouda N, Tanchot C, et al. VEGF-A modulates expression of inhibitory checkpoints on CD8 + T cells in tumors. J Exp Med. 2015;212:139–48.
21. Tang H, Wang Y, Chlewicki Lukasz K, Zhang Y, Guo J, Liang W, Wang J, Wang X, Fu Y-X. Facilitating T cell infiltration in Tumor Microenvironment overcomes resistance to PD-L1 blockade. Cancer Cell. 2016;30:500.
22. Ferrara N, Kerbel RS. Angiogenesis as a therapeutic target. Nature. 2005;438:967–74.
23. Siemann DW, Shi W. Efficacy of combined antiangiogenic and vascular disrupting agents in treatment of solid tumors. Int J Radiation Oncology*Biology*Physics. 2004;60:1233–40.
24. Bergers G, Hanahan D. Modes of resistance to anti-angiogenic therapy. Nat Rev Cancer. 2008;8:592–603.
25. Ebos JML, Kerbel RS. Antiangiogenic therapy: impact on invasion, disease progression, and metastasis. Nat Reviews Clin Oncol. 2011;8:210–21.
26. Wolchok JD, Chiarion-Sileni V, Gonzalez R, Rutkowski P, Grob J-J, Cowey CL, Lao CD, Wagstaff J, Schadendorf D, Ferrucci PF, et al. Overall survival with combined Nivolumab and Ipilimumab in Advanced Melanoma. N Engl J Med. 2017;377:1345–56.
27. Motzer RJ, Escudier B, McDermott DF, George S, Hammers HJ, Srinivas S, Tykodi SS, Sosman JA, Procopio G, Plimack ER, et al. Nivolumab versus Everolimus in Advanced Renal-Cell Carcinoma. N Engl J Med. 2015;373:1803–13.
28. Chen DS, Mellman I. Elements of cancer immunity and the cancer–immune set point. Nature. 2017;541:321–30.
29. Sharma P, Hu-Lieskovan S, Wargo JA, Ribas A. Primary, adaptive, and Acquired Resistance to Cancer Immunotherapy. Cell. 2017;168:707–23.
30. Topalian SL, Taube JM, Anders RA, Pardoll DM. Mechanism-driven biomarkers to guide immune checkpoint blockade in cancer therapy. Nat Rev Cancer. 2016;16:275–87.
31. Tian L, Goldstein A, Wang H, Ching Lo H, Sun Kim I, Welte T, Sheng K, Dobrolecki LE, Zhang X, Putluri N, et al. Mutual regulation of tumour vessel normalization and immunostimulatory reprogramming. Nature. 2017;544:250–4.
32. Sun C, Mezzadra R, Schumacher TN. Regulation and function of the PD-L1 checkpoint. Immunity. 2018;48:434–52.
33. Erickson JJ, Gilchuk P, Hastings AK, Tollefson SJ, Johnson M, Downing MB, Boyd KL, Johnson JE, Kim AS, Joyce S, Williams JV. Viral acute lower respiratory infections impair CD8 + T cells through PD-1. J Clin Invest. 2012;122:2967–82.
34. Watanabe H, Matsushita Y, Tamura K, Motoyama D, Sugiyama T, Otsuka A, Miyake H. Assessments of therapeutic effects according to timings for combined therapy with axitinib and immune check point inhibitor in a mouse renal cell carcinoma model. Sci Rep. 2023;13:11361.
35. Gao H, Qian J, Cao S, Yang Z, Pang Z, Pan S, Fan L, Xi Z, Jiang X, Zhang Q. Precise glioma targeting of and penetration by aptamer and peptide dual-functioned nanoparticles. Biomaterials. 2012;33:5115–23.
36. Liu Z-J, Boulina M, Ting A, Wang D, Moller M, Shao H. A novel stromal fibroblast-modulated 3D Tumor Spheroid Model for studying Tumor-Stroma Interaction and Drug Discovery. J Vis Exp. 2020;156:e60660.
37. Wang S, Raybuck A, Shiuan E, Cho SH, Wang Q, Brantley-Sieders DM, Edwards D, Allaman MM, Nathan J, Wilson KT et al. Selective inhibition of mTORC1 in tumor vessels increases antitumor immunity. JCI Insight. 2020;5:e139237.
38. Hong S, Zheng D-W, Zhang C, Huang Q-X, Cheng S-X, Zhang X-Z. Vascular disrupting agent induced aggregation of gold nanoparticles for photothermally enhanced tumor vascular disruption. Sci Adv. 2020;6: eabb0020.
39. Rinchai D, Verzoni E, Huber V, Cova A, Squarcina P, De Cecco L, de Braud F, Ratta R, Dugo M, Lalli L et al. Integrated transcriptional-phenotypic analysis

captures systemic immunomodulation following antiangiogenic therapy in renal cell carcinoma patients. Clin Translational Med. 2021;11:e434.
40. Kondo Y, Suzuki S, Takahara T, Ono S, Goto M, Miyabe S, Sugita Y, Ogawa T, Ito H, Satou A, et al. Improving function of cytotoxic T-lymphocytes by transforming growth factor-β inhibitor in oral squamous cell carcinoma. Cancer Sci. 2021;112:4037–49.
41. Yang Y, Yang Y, Xie X, Cai X, Zhang H, Gong W, Wang Z, Mei X. PEGylated liposomes with NGR ligand and heat-activable cell-penetrating peptide–doxorubicin conjugate for tumor-specific therapy. Biomaterials. 2014;35:4368–81.
42. Kang L, Fan B, Sun P, Huang W, Jin M, Wang Q, Gao Z. An effective tumor-targeting strategy utilizing hypoxia-sensitive siRNA delivery system for improved anti-tumor outcome. Acta Biomater. 2016;44:341–54.

Publisher's note